Designing, Physiochemical Confirmation, Evaluation of Biological and *in-silico* Potential of Triorganotin(IV) Complexes

Bibi Hanifa[a], Muhammad Sirajuddin[a,*], Edward R. T. Tiekink[b], Ishaq Khan[c], Maciej Kubicki[d], Ahmed Bari[e]

[a] Department of Chemistry, University of Science & Technology Bannu 28100, Pakistan

[b] Research Centre for Crystalline Materials, School of Medical and Life Sciences, Sunway University, No. 5 Jalan Universiti, Bandar Sunway 47500, Selangor Darul Ehsan, Malaysia

[c] Cancer Cell Culture & Precision Oncomedicine Lab, Institute of Basic Medical Sciences, Khyber Medical University, Peshawar 25100, Pakistan

[d] Department of Chemistry, Adam Mickiewicz University in Poznan, Poznan 61-712, Poland

[e] Department of Pharmaceutical Chemistry, College of Pharmacy, King Saud University, Riyadh 11451, Saudi Arabia

For correspondence: m.siraj09@gmail.com (Muhammad Sirajuddin)

Abstract

FTIR, NMR, CHN and single crystal X-ray crystallography were used to validate a series of three new triorganotin(IV) carboxylate complexes, $R_3Sn(L)$ for R = Methyl (**1**), *n*-Butyl (**2**) and Phenyl (**3**), obtained from LH = 4-[(2,5-dimethoxyphenyl)carbamoyl]butanoic acid. The coupling constant and $\theta_{C\text{-}Sn\text{-}C}$ values in solution-state NMR data suggest a 5-coordinated environment around the Sn centre. In the crystal of **1**, the carboxylate is bidentate bridging leading to a zigzag chain with the Sn centre having a distorted trigonal-bipyramidal geometry. The compounds were evaluated for their interaction with salmon sperm DNA and found that they interact through an intercalative mode resulting in hypochromism and bathochromic shift as confirmed by the UV-visible spectroscopic and viscometric techniques. The findings of anti-microbial activity performed on five bacterial and two fungus strains demonstrate that some of the compounds exhibit >80% inhibition of certain bacteria and >100% inhibition of certain fungal strains. The compounds were also evaluated for cell viability tested on human embryonic kidney cell (HEC-239) and human red blood cells (RBC). The anti-cancer potential of the compounds was assessed using *cis*-platin as a standard against human malignant glioma U87 (MG-U87) cell lines, and **1** was shown to be the most potent (IC_{50}: 148.979 µM) at a 50 µM dose. The DPPH anti-oxidant activity results revealed a 91% maximum scavenging activity for **1**. The compounds follow the

principles of drug-likeness and have good bioavailability potential, according to an *in silico* analysis conducted using the SwissADME webserver.

Keywords: Organotin(IV) complexes; DNA intercalation; anti-cancer potential; haemolysis activity; anti-microbial activity; DPPH scavenging; *in silico* study

1. Introduction

Due to major biocidal and industrial applications, carboxylic acid ligands have piqued interest in the last few decades [1]. They produce a variety of supramolecular structures due to their flexible binding nature. In complexation, the carboxylate moiety can attach to metal either in ionic or covalent modes. In the latter case, coordination can take place in monodentate, bridging, or bidentate (syn-syn or syn-anti) modes [2, 3]. By stabilising polynuclear metal complexes, the carboxylate moiety as a ligand is useful in the preparation of coordination and organometallic complexes with favourable characteristics [4]. Metal carboxylate complexes are utilised in a variety of sectors, including rubber adhesives, paints, inks, coatings, lubricants and grease driers, to name a few. Polymerisation, oxidation, esterification, hydrogenation, and condensation are among the chemical reactions for which they are utilised as catalysts [5].

Among the metal carboxylate complexes, Organotin(IV) carboxylates have a diverse variety of biological and non-biological applications, owing to the relatively greater atomic radius, high ability for accepting electron and availability of empty 5d orbital, to name a few characteristics that distinguish tin as a unique and multipurpose element [6].

The non-biological aspects of some organotin carboxylates include for example: photostabiliser for polyvinyl chloride (PVC) [7], Sensing and photocatalytic properties [8] catalyst for transesterification of biodiesel formation [9] etc.

The biological aspects of organotin(IV) carboxylates, particularly triorganotin(IV) complexes, including anti-bacterial, anti-leishmanial and anti-cancer properties have been studied extensively [10-14]. The main cause of the death Worldwide is the cancer which requires potent drugs for effective treatment. Compounds capable of being used as anti-cancer drugs must react with DNA either in covalent or non-covalent mode resulting in alteration or inhibition of regular DNA function. Those compounds which bind to the DNA nitrogenous bases lead to the inhibition of cell division through interference with DNA replication and transcription processes. Another possible mechanism for anti-cancer activity is that proliferation of the cells is halted by affecting the multienzyme complexes which are accountable for the DNA replication and transcription [15-17].

Organotin(IV) complexes, for example, have exhibited substantial anti-tumour potential/activity *in vitro*/*in vivo* and have emerged as biologically-active metallopharmaceuticals [18]. In this context, the anti-cancer potential of organotin(IV) carboxylates which bind to DNA most likely function *via* intercalative interactions [19].

Novel antimicrobial agents are also desperately needed to tackle the growing threat of widespread antimicrobial resistance. With a medication pipeline that is primarily made up of variants of well-known antibiotics, new anti-biotic classes is highly required. Metal complexes are being tested in clinical trials for cancer, malaria, and neurological illnesses. While metal-containing compounds in The Community for Antimicrobial Drug Discovery (CO-ADD) database have a much greater success rate than free ligands, petite consideration has been paid to their potential as antimicrobial medicines [20].

A facile and cost-effective approach for synthesising glutaric anhydride-based carboxylic acid ligand is presented herein, needing only room temperature conditions and a maximum reaction time of 3-5 minutes. The synthesised glutaric acid-amide based carboxylate ligand was reacted with three triorganotin precursors to form the respective triorganotin(IV) carboxylate complexes. Biological evaluation including DNA binding, anti-cancer potential, anti-microbial, haemolysis activity and anti-oxidant potentials are reported in this work. Moreover, an *in-silico* analysis of the new compounds was also carried out.

2. Materials and Methods

The precursors 2,5-dimethoxyaniline and glutaric anhydride were purchased from Macklin. Solvents of high degree of purity were purchased from Sigma. The melting points were determined on a BioCote melting point apparatus. The CHN compositions were determined on a PerkinElmer CHNS 2400 instrument. The FTIR spectra were measured on a Thermo Nicolet-6700 spectrophotometer from 4000 to 400 cm^{-1}. The ^{1}H and $^{13}C\{^{1}H\}$ NMR spectra were recorded in DMSO-d_6 and $CDCl_3$ solutions on a Bruker Avance 500-MHz NMR spectrometer. The DNA binding experiments were performed using a UH-5300 UV/Vis. spectrophotometer and a PSL ASTM Ubbelohde viscometer. DPPH activity was also performed using UH-5300 UV/Vis. Spectrophotometer. The GC-MS spectrum of the ligand **LH** was obtained using a Thermo Scientific TRACE™ 1310 Gas Chromatograph and Thermo Scientific ISQ™ Series Quadrupole GC-MS with conditions: carrier gas: helium; column gas flow: 1.2 mL/s; constant flow; injection mode: splitless injection; column: Agilent HP 5MS, (30 m x 0.25 mm x 25 μm); inlet temp.: 270

°C; oven temperature program: 40 °C (1 min) at 10 °C/min to 300 °C (7 min); transfer line temp.: 300 °C; solvent delay: 2.5 min; ionization energy: 70 eV; ion source temp.: 230 °C; mass range: 35–550 amu, scan rate: 3 scan/s; software: Xcalibur

2.1. X-ray crystallography

X-ray intensity data were collected at 100 K for light brown **LH** (0.06 × 0.11 × 0.14 mm) on a Rigaku/Oxford Diffraction XtaLAB Synergy diffractometer (Dualflex, AtlasS2) fitted with a CuKα radiation source (λ = 1.54184 Å) and for yellow-brown **1** (0.07 × 0.12 × 0.25 mm) on a Rigaku SuperNova four-circle diffractometer with Atlas CCD detector, equipped with MoKα radiation (λ = 0.71073 Å). The data sets were processed, including correcting for absorption effects, with CrysAlis PRO [21]. The structures were solved with SHELXS (**LH**)/SHELXT (**1**) [22] and refined by a full-matrix least-squares procedure on F^2 employing SHELXL [23]. The non-hydrogen atoms were refined with anisotropic displacement parameters and carbon-bound hydrogen atoms were placed in their idealised positions. For **LH**, the O- and N-bound atoms were located from a difference map and refined with O–H = 0.84±0.01 and N–H = 0.88±0.01 Å distance restraints, and with U_{iso}(H) set to 1.5U_{equiv}(O) and 1.2U_{equiv}(N), respectively. For **1**, the N–H distance was fixed at 0.88 Å with U_{iso}(H) = 1.2U_{equiv}(N). A weighting scheme of the form $w = 1/[\sigma^2(F_o^2) + (aP)^2 + bP]$, where $P = (F_o^2 + 2F_c^2)/3$, was introduced in each refinement. The programs ORTEP-3 for Windows [24] DIAMOND [25] and PLATON [26] were also used in the analysis of the crystallography. Crystal data and refinement details are given in Table 1.

Table 1. Crystal data, data collection and refinement details for **LH** and **1**

Compound	**LH**	**1**
Formula	$C_{13}H_{17}NO_5$	$C_{16}H_{25}NO_5Sn$
Formula weight	267.27	430.06
Crystal system	monoclinic	Orthorhombic
Space group	$P2_1/n$	*Pbca*
a (Å)	7.5948(1)	13.5588(2)
b (Å)	37.6944(4)	9.32663(13)
c (Å)	9.4563(2)	29.3940(4)
β (°)	113.126(2)	90
V (Å^3), Z	2489.62(8), 8	3717.10(9), 8
D_x (g cm^{-3})	1.426	1.537
F(000), μ (mm^{-1})	1136, 0.923	1744, 1.397
Reflections:		
Collected	31119	9692
unique (R_{int})	4419 (0.021)	3731 (0.020)
with $I > 2\sigma(I)$	4065	3393
θ_{max} (°), 100% completeness	67.1	25.0
$R(F)$ [$I > 2\sigma(I)$]	0.042	0.027
a, *b* in weighting scheme	0.413, 1.780	0.019, 6.164
$wR(F^2)$ [all data]	0.105	0.060
max/min Δρ (e·Å^{-3})	0.18/-0.25	0.70/-0.69
CCDC number	2130960	2130961

2.2. Synthesis

The reactions and structures are as depicted in Scheme 1. Glutaric anhydride (1.141 g, 10 mmol), dissolved in toluene (25 mL), was treated at room temperature with 2,5-dimethoxyaniline (1.532 g, 10 mmol) also dissolved in toluene (25 mL). After mixing the reactants, a precipitate appeared after a few mins. To remove any unreacted reactants, the precipitate was washed with toluene, followed by distilled H_2O to remove any glutaric acid. The product was then air-dried to get the desired compound, 4-[(2,5-dimethoxyphenyl)carbamoyl]butanoic acid (**LH**) [27-32]. Recrystallization of the product was from its acetone/ethanol (1:1 *v*/*v*) solution.

LH was then transformed into its sodium salt, **NaL** by treating its aqueous suspension with $NaHCO_{3(aq)}$. The desired solid product was acquired after rotary evaporation of the solvent.

NaL was reacted with R_3SnCl (R = CH_3, *n*-C_4H_9, C_6H_5) in 1:1 molar ratio in toluene (50 mL) and refluxing the mixture for 6-8 h. The anticipated compounds were recrystallized from acetone/ethanol (1:1 *v*/*v*) solution.

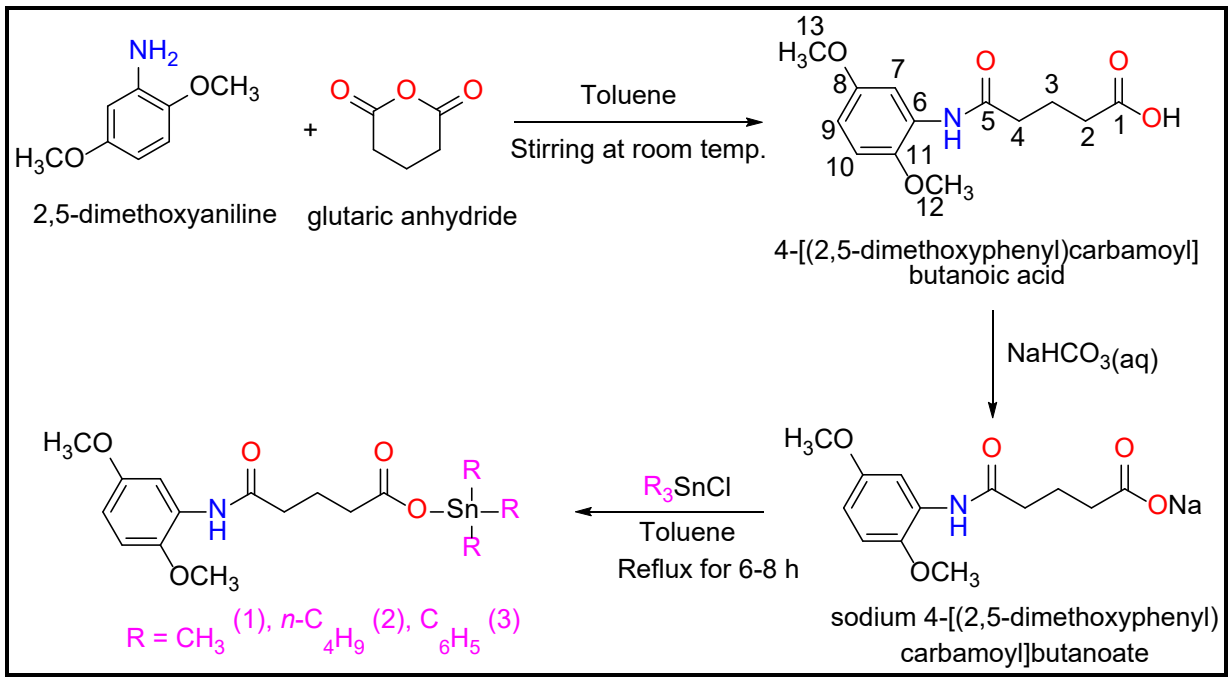

Scheme 1. Schematic representation of **LH** and its triorganotin(IV) complexes along with atom numbering for NMR data interpretation.

2.3. Anti-microbial screening

The anti-bacterial data against five bacterial strains (*S. aureus*, *E. coli*, *K. pneumoniae*, *A. baumannii* and *P. aeruginosa*) as specified in Table 2, was determined by CO-ADD following the Cooper *et al* [20, 33] well-established procedure. At 37 °C overnight, all bacteria were grown in cation-adjusted Mueller Hinton broth (CAMHB). After that, a sample of each culture was diluted 40 times in fresh broth and incubated for 1.5-3 hours at 37 °C. The mid-log phase cultures were then diluted and fed to each well of the compound-containing plates, resulting in a cell density of 5 x 10^5 CFU/mL. Plates were covered and incubated at 37 °C without shaking for 18 hours. Using a Tecan M1000 Pro monochromator plate reader, the suppression of bacterial growth was evaluated by measuring the absorbance at 600 nm (OD_{600}). For each well, the percentage of growth inhibition was computed using the same plate's negative control (media only) and positive control (bacteria without inhibitors) as references. Modified Z-scores were used in the screening to determine the significance of the inhibition values, which were calculated using the median and mean absolute deviation (MAD) of the samples (no controls) on the same plate. Active samples

had inhibition values greater than 80% and Z-scores greater than 2.5 for either replicate (n = 2 on distinct plates), while inactive samples had inhibition values less than 50.9-79.9% and Z-scores less than 2.5 [33].

The anti-fungal data against two fungal strains (*C. neoformans* and *C. albicans*) was determined by CO-ADD following the Cooper *et al* [20, 33] well-established procedure. Fungi strains were grown for three days at 30°C on Yeast Extract-Peptone Dextrose (YPD) agar. Five colonies were used to make a yeast slurry containing 1 x 10^6 to 5 x 10^6 CFU/mL (as assessed by OD_{530}). Following that, each suspension was diluted and added to each well of the compound-containing plates, resulting in a final cell density of 2.5 x 10^3 CFU/mL and a total volume of 50 µL. All plates were covered and incubated at 35 °C for 24 h without shaking. Growth inhibition of *C. albicans* was determined measuring absorbance at 530 nm (OD_{530}), while the growth inhibition of *C. neoformans* was determined measuring the difference in absorbance between 600 and 570 nm ($OD_{600-570}$), after the addition of resazurin (0.001% final concentration) and incubation at 35 °C for an additional 2 h. The absorbance was measured using a Biotek Synergy HTX plate reader. For each well, the percentage of growth inhibition was estimated using the negative control (media only) and positive control (bacteria without inhibitors) as references on the same plate.

2.4. Cytotoxicity assay

The cytotoxicity of the tested compounds was determined by CO-ADD against Human embryonic kidney cells (HEK-293) following the Cooper *et al*., [20, 33] method. In a Neubauer haemocytometer, HEK-293 cells were manually counted and then plated in 384-well plates containing the compounds at a density of 5000 cells/well in a total volume of 50 µL. The cells were grown in DMEM (Dulbecco's Modified Eagle Medium) supplemented with 10% FBS (Fetal bovine serum), and they were treated with the compounds for 20 hours at 37 °C in 5% CO_2. After adding 5 µL of 25 g/mL resazurin (2.3 g/mL final concentration) and incubating for another 3 h at 37 °C in 5% CO_2, cytotoxicity (or cell viability) was measured by fluorescence, ex: 560/10 nm, em: 590/10 nm ($F_{560/590}$). The fluorescence intensity was measured using an automatic gain calculation on a Tecan M1000 Pro monochromator plate reader. Curve fitting the inhibition values vs log(concentration) using a sigmoidal dose-response function with variable fitting values for bottom, top, and slope yielded the CC_{50} (concentration at 50% cytotoxicity). D_{Max} also indicates any compounds with partial cytotoxicity, as well as the maximum percentage of cytotoxicity.

The curve fitting was implemented using Pipeline Pilot's dose-response component, resulting in similar values to curve fitting tools such as GraphPad's Prism and IDBS's XlFit. In addition, the maximal percentage of cytotoxicity is reported as D_{Max}, indicating any compounds with partial cytotoxicity. Cytotoxic samples were classified by $CC_{50} \leq 32$ µg/mL or $CC_{50} \leq 10$ µM in either replicate (n = 2 on different plates). In addition, samples were flagged as partially cytotoxic if $D_{Max} \geq 50\%$, even with CC_{50} > the maximum tested concentration. Tamoxifen was used as a positive cytotoxicity standard.

2.5. Haemolysis assay

The haemolysis activity of the tested compounds was determined by CO-ADD against human red blood cells (RBC) following the Cooper *et al*., [20, 33] method. Human whole blood was washed thrice with three volumes of 0.9% NaCl and then resuspended in 0.9% NaCl to a concentration of 0.5 x 10^8 cells/mL, as determined by manual cell count in a Neubauer haemocytometer. The washed cells were then added to the 384-well compound-containing plates to a final volume of 50 µL. After 10 mins shaking on a plate shaker, the plates were then incubated for 1 h at 37 °C. After incubation, the plates were centrifuged at 1000 g for 10 min to pellet cells and debris, 25 µL of the supernatant was then transferred to a polystyrene 384-well assay plate. Haemolysis was determined by measuring the supernatant absorbance at 405 mm (OD_{405}). The absorbance was measured using a Tecan M1000 Pro monochromator plate reader. HC_{10} and HC_{50} (concentration at 10% and 50% haemolysis, respectively) were calculated by curve fitting the inhibition values *vs* log(concentration) using a sigmoidal dose-response function with variable fitting values for top, bottom and slope. In addition, the maximal percentage of haemolysis is reported as D_{Max}, indicating any compound with partial haemolysis. Haemolysis samples were classified by $HC_{10} \leq 32$ µg/mL in either replicate (n = 2 on different plates). In addition, samples were flagged as partial haemolytic if $D_{Max} \geq 50\%$, even with HC_{10} > the maximum tested concentration. Melittin was used as a positive haemolytic standard.

Table 2. Information of the bacterial and fungal strain investigated in the present study

Abbr.	Code	Name	Description	Strain	Organism	Type
Sa	GP_020	*Staphylococcus aureus*	MRSA	ATCC 43300	Bacteria	G+ve
Ec	GN_001	*Escherichia coli*	FDA control	ATCC 25922	Bacteria	G-ve
Kp	GN_003	*Klebsiella pneumoniae*	MDR	ATCC 700603	Bacteria	G-ve
Ab	GN_034	*Acinetobacter baumannii*	Type strain	ATCC 19606	Bacteria	G-ve
Pa	GN_042	*Pseudomonas aeruginosa*	Type strain	ATCC 27853	Bacteria	G-ve
Ca	FG_001	*Candida albicans*	CLSI reference	ATCC 90028	Fungi	Yeast
Cn	FG_002	Cryptococcus *neoformans var. grubii*	Type strain	H99; ATCC 208821	Fungi	Yeast
Hk	MA_007	Human embryonic kidney cells	HEK-293	ATCC CRL-1573	Human	Eukaryotes
Hm	HA_150	Human red blood cells	RBC		Human	Eukaryotes

Standards

Sample name	Sample ID	Full MW	Stock Conc. (mg/mL)	Solvent	Source
Colistin-sulphate	MCC_000094:02	1400.63	10.0	DMSO	Sigma; C4461
Vancomycin-HCl	MCC_000095:02	485.71	10.0	DMSO	Sigma; 861987
Fluconazole	MCC_008383:01	306.27	2.56	DMSO	Sigma; F8929

2.6. Cytotoxicity assay on MG-U87 cells

The synthesized compounds were tested against human malignant glioma U87 (MG-U87) cell lines following the procedure reported by Nemat *et al* [34]. 10,000 cells per well were plated on 96 wells plate. The plate was incubated and monitored for confluency and infection. Once the

wells were 90-100% confluent, drug (compounds prepared in DMSO) was applied. The cells were treated in triplicates with various concentrations of the compounds at doses of 0 μM (untreated control), 12.5, 25, 50, 100, 200 and 400 μM after 24 h growth. The untreated cells were used as a control in triplicates. After drug application, the plate was incubated for two days in a humidified atmosphere of CO_2 incubation at 37°C and monitored after 24 h and 48 h intervals to find a dosage concentration that might stop the cells from growing by 50% (IC_{50}). This resulted in having different percentages of dead cells and alive cell in different wells. For reading and visualization purpose, the plate was washed with PBS and fixation was done with formalin. After fixation staining with crystal violet dye was performed and plate was analysed on ELSA at 630 nm and 490 nm. The readings were recorded and IC_{50} value was determined on excel. *Cis*-platin was used as a standard drug.

2.7. DNA binding assay by UV-visible spectroscopy and viscometry

A 2 mg of the sodium salt of SS-DNA was dissolved in distilled water and stirred at 25 °C overnight. The concentration of the DNA solution was determined on a UH-5300 UV/Vis. spectrophotometer using based on $\varepsilon = 6600\ M^{-1}.cm^{-1}$ and found to be 1.4×10^{-4} M. The nature of DNA free from protein was checked from its absorbance ratio $A_{260}/A_{280} = 1.8$. A solution of each of **LH** and **1-3** (1 mM) was prepared in 70% absolute EtOH. During the DNA binding study, the concentration of **LH** and **1-3** was kept constant while that of the DNA was changed [35-37].

The simplest and easiest way for knowing the DNA binding mode is the viscosity method. In this method, the viscosity was determined with the help of an Ubbelohde viscometer at a room temperature and the result was plotted between $[(\eta/\eta_o)^{1/3}]$ on y-axis and a binding ratio [(compound)/(DNA)] on x-axis. Here η_o and η show the viscosity of DNA in the absence and presence of **LH** and **1-3**, respectively [38-40].

2.8. DPPH scavenging activity

DPPH solution was prepared by dissolving its 3.94 mg in 100 mL of MeOH. The DPPH and solutions of **1-3** were prepared as follows: to methanolic solutions of DPPH (2800 μL) was added 0.2 μL of **1-3** (also prepared in methanol) with concentrations of **1-3** ranging from 10 to 150 mg/mL. The decrease in DPPH absorbance was noted at 517 nm after 10 mins *via* UH-5300 UV/Vis. spectrophotometer. The same protocol was followed for the well-known anti-oxidant standard, ascorbic acid. All the measurements were performed in triplicate and average results

reported. The percent scavenging activity of screened compounds was measured using the below given equation: [41, 42].

$$\%\ \text{Scavenging activity} = \frac{A_o - A_s}{A_o}$$

A_o and A_s represent the DPPH absorbance in the absence and presence of sample (**LH** and **1-3**), respectively.

2.9. Drug-likeness and ADME studies

SwissADME webserver was used to determine the ADME properties such as physicochemical, pharmacokinetics and drug similarity properties of the evaluated compounds. With the help of 6 different parameters, the oral bioavailability of the screened samples was also checked in a radar image. Similarly the absorption potential of the tested compounds in the gastrointestinal system was checked using the BOILED-Egg model [43, 44].

3. Results and discussion

The carboxylic acid, 4-[(2,5-dimethoxyphenyl)carbamoyl]butanoic acid (**LH**), was synthesised from the 1:1 (nucleophilic addition) reaction of glutaric anhydride with 2,5-dimethoxyaniline. It was then changed into its sodium salt, **NaL**, which served as the precursor for the synthesis of the triorganotin(IV) complexes (**1-3**). The solubility of the synthesized compounds was checked in common organic solvents such as MeOH, EtOH, DMSO, acetone and chloroform and found freely soluble in these solvents. The synthesized compounds were also air-stable. The physical and CHN data are depicted in Table 3. Details of the spectroscopic and crystallographic characterisation are given below. In addition, certain medicinal potential, namely DNA binding, anti-microbial, cytotoxicity anti-oxidant potentials and the theoretical evaluation of medicinally relevant attributes are reported.

Table 3. Physical, CHN and FT-IR data of **LH** and complexes **1-3**

Comp.	M.P (°C)	Formula	M.Wt	Colour	CHN data in % (calc./found)		
					C	H	N
LH	108-110	$C_{13}H_{17}NO_5$	267.28	Light brown	58.42/58.33	6.41/6.15	5.24/5.10
1	170-172	$C_{16}H_{25}NO_5Sn$	430.1	Creamy	44.68/44.21	5.86/5.91	3.26/3.40
2	52-54	$C_{25}H_{43}NO_5Sn$	556.3	Brown	53.97/54.01	7.79/7.81	2.52/2.56
3	96-98	$C_{31}H_{31}NO_5Sn$	616.3	Yellow	60.42/60.12	5.07/5.11	2.27/2.35

FTIR data (ν, cm^{-1})

	OH	$C{=}O_{amide}$	NH	$C{=}O_{carboxyl}$	COO_{asym}	COO_{sym}	Δν	Sn-O	Sn-C
LH	3252	1671	3376	1757	-	-	-	-	-
1	-	1655	3376	-	1535	1300	235	477	546
2	-	1671	3427	-	1527	1310	217	485	577
3	-	1683	3428	-	1527	1320	207	455	583

3.1. FTIR

Table 3 describes the important functional groups. A strong stretching vibration peak in the spectrum of **LH** at 1757 cm^{-1} was ascribed to the carboxylic acid carbonyl functional group. The characteristics NH stretching vibration peak appeared at 3376, 3418, 3427 and 3428 cm^{-1} in **LH** and **1-3** spectra, respectively. Another strong peak attributed to the stretching vibration of amide carbonyl functional group was detected at 1671, 1654, 1691 and 1683 cm^{-1} in **LH** and **1-3** spectra, respectively.

The coordination of the ligand was proven by the emergence of the vibration band ν(C–O) at 1273-1280 cm^{-1} in the spectra of the **1-3**, which was caused by the deprotonation of the OH and subsequent coordination to the tin atom. The absence of vibrational bands associated with the carboxylic acid indicated carboxylate synthesis and coordination to the tin centre. The existence of two strong vibrational bands with distinct absorptions in the range of 1300-1320 cm^{-1} and 1527-1535 cm^{-1}, which correspond to the symmetric (νCOO_s) and asymmetric (νCOO_{as}) stretching vibrational modes of the carboxyl group, respectively, promoted the formation of the Sn–O bond [46]. The $\Delta\nu = \nu_{as}(OCO) - \nu_s(OCO)$, provides important evidence for the Sn-carboxyl coordination mode [47]. For chelating bidentate coordination, $\Delta\nu \leq 100$ cm^{-1}, for bridging bidentate

coordination, $\Delta\nu$ = 100-150 cm^{-1}, and for ionic coordination, $\Delta\nu \geq 200$ cm^{-1}, according to Nelson and coworkers [48]. $\Delta\nu$ calculated for **1-3** are: 235, 217 and 207 cm^{-1}, respectively. The development of a covalent metal oxygen connection and a monodentate coordination mode of the carboxylic group linked to the tin atom results in a $\Delta\nu$ (COO) > 200 cm^{-1} [48]. The IR spectra of the **1-3** show a peak due to Sn–O in the range of 455-485 cm^{-1} and a peak due to Sn–C in the range of 546-583 cm^{-1}, indicating the production of the subsequent organotin complexes [49, 50].

3.2. NMR

A singlet at δ 11.07 ppm was assigned to the carboxylic acid OH confirming the existence of the carboxylic acid residue in the ^{1}H NMR spectrum of **LH**. After complexation with Sn, this resonance was absent in spectra of **1-3**. The resonance of the NH proton was observed as a singlet in the range 8.07-8.91 ppm in the spectra of **LH** and **1-3**. Additional resonances, multiplicity and integration, are as expected, see Table 4. The H-α (Sn-CH_3) in **1** appeared as a sharp singlet at 0.57 ppm with satellites having $^{2}J(^{119}Sn\text{-}^{1}H)$ coupling of 69 Hz. The $^{2}J(^{119}Sn\text{-}^{1}H)$ coupling value was used to calculate the $\theta_{C\text{-}Sn\text{-}C}$ (117°) by means of Lockhart equation [51].

The most notable features in the $^{13}C\{^{1}H\}$ NMR spectra of **LH** and **1-3** is downfield resonance of carboxylic acid (C-1) at δ 178.5, 176.9 and 179.9 ppm (**1-3**) compared to that for **LH** at δ 174.9 ppm as a result of electron density shifted from **LH** to Sn(IV) centre. The resonances of the remaining nuclei fall in their anticipated regions [52] as detailed in Table 4.

Some additional resonances for alky/aryl groups attached to the Sn centre were present in the spectra of **1-3** as tabulated in Table 4. In $^{13}C\{^{1}H\}$ NMR spectrum of **1**, C-α (Sn-CH_3) appeared as δ -2.5 ppm with satellites having A $^{1}J(^{119}Sn\text{-}^{13}C)$ coupling of 520 Hz give a $\theta_{C\text{-}Sn\text{-}C}$ (calculated from Lockhart equation) value of 122°. For **2** and **3**, the values of $^{1}J(^{119}Sn\text{-}^{13}C)$ coupling and $\theta_{C\text{-}Sn\text{-}C}$ are 479 Hz, 123° and 750 Hz, 123°, respectively [53].

Table 4. $^{1}H/^{13}C\{^{1}H\}$ NMR data (δ in ppm and *J* value in Hz) for **LH** and complexes **1-3**

H nucleus	LH	Complex 1	Complex 2	Complex 3
OH	11.07	-	-	-
2	2.29 (t, 7.5 Hz)	2.48 (t, 7.5 Hz)	2.39 (t, 7 Hz)	2.56 (t, 7.3)
3	1.82 (q, 7.5 Hz)	2.05 (q, 7.3 Hz)	1.75 (q, 7 Hz)	2.10 (q, 7.3)
4	2.20 (t, 7.5 Hz)	2.44 (t, 7 Hz)	2.11 (t, 7 Hz)	2.42 (t, 7.3)
NH	8. 07 (s)	8.15 (s)	8.91 (s)	8.14 (s)
7	7.80 (s)	7.86 (s)	7.73 (s)	7.51 (s)
9	6.34 (d, 10 Hz)	6.57 (d, 8.5 Hz)	6. 59 (d, 5 Hz)	6.59 (d, 5 Hz)
10	6.59 (d, 10 Hz)	6.79 (d, 8.5 Hz)	6.92 (d, 5 Hz)	6.79 (d, 5 Hz)
12	3. 64 (s)	3.85 (s)	3.77 (s)	3.85 (s)
13	3.56 (s)	3.79 (s)	3.68 (s)	3.77 (s)
α	-	0.57 [69 Hz/117°]	1.08 (t, 7 Hz)	-
β	-	-	1.58 (q, 7 Hz)	7.42-7.75 (Sn-Ph)
γ	-	-	1.30 (m)	-
δ	-	-	0.87 (t, 7 Hz)	-
C nucleus		**$^{13}C\{^{1}H\}$**		
1	174.9	178.5	176.9	179.9
2	36.5	37.1	36.4	36.9
3	20.6	21.5	22.5	21.5
4	33.0	33.9	35.7	33.3
5	170.5	170.7	171.7	170.5
6	128.2	128.4	128.8	128.4
7	106.3	105.8	108.1	105.8
8	153.5	153.9	153.4	153.9
9	107.9	108.6	108.4	108.6
10	110.7	110.7	112.1	110.7
11	142.1	141.9	143.7	141.9
12	56.1	56.2	56.6	56.1
12'	55.4	55.7	55.7	55.8
α	-	-2.5 [520 Hz /122°]	19.7 [479/123°]	138.3
β	-	-	26.9 [74 Hz]	136.8 [750 Hz /123°]
γ	-	-	28.2 [28 Hz]	128.9 [65 Hz]
δ	-	-	14.1	130.2

3.3. X-ray crystallography

3.3.1 Molecular structures

Figure 1 describes the molecular structure of **LH** comprising of two independent molecules with asymmetric crystallographic unit. Selected geometric parameters are collated in Table 5. The independent molecules present very similar geometric parameters as seen in the root-mean-square values for bond lengths and angles, as calculated in PLATON [26] of 0.0024 Å and 0.216°, respectively. The disparity in the C–O bond lengths confirm the carboxylic acid assignment. An *anti*-conformation is noted for the carbonyl-O and amide-H atoms comprising the amide residue. In terms of conformation, an all-*trans* conformation is noted for the backbone of each molecule with the greatest difference, *i.e. ca* 12°, seen in the values of the C3–C4–C5–N1 torsion angles. The overall planarity of the molecule is seen in the values of the dihedral angles between the carboxylic acid and arene planes, *i.e.* 4.09(11) and 9.29(19)° for molecules a and b, respectively. A partial explanation for the observed planarity in the molecules stems from the presence of intramolecular amide-N–H···O(methoxy) hydrogen bonds, Table 6.

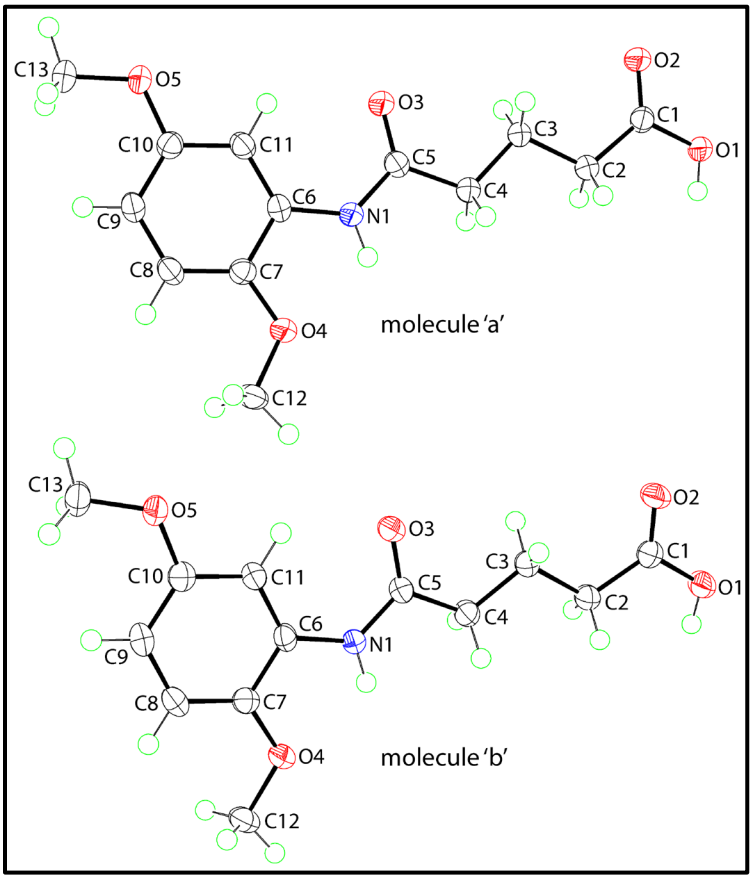

Fig. 1. The molecular structures of the two independent molecules of **LH**, showing the atom-labelling schemes and displacement ellipsoids at the 70% probability level.

Table 5. Selected geometric parameters (Å, °) for **LH** and **1**

Parameter	**LH**, molecule a	**LH**, molecule b	**1**
C1–O1	1.347(2)	1.349(2)	1.273(3)
C1–O2	1.202(2)	1.202(2)	1.257(3)
C5–O3	1.227(2)	1.226(2)	1.229(3)
C5–N1	1.361(2)	1.360(2)	1.356(3)
O1–C1–C2–C3	-179.80(14)	177.63(15)	7.8(4)
C1–C2–C3–C4	-178.49(13)	176.89(15)	-176.6(2)
C2–C3–C4–C5	-179.12(13)	175.84(14)	170.1(2)
C3–C4–C5–N1	-175.97(14)	-163.67(14)	154.5(2)
C4–C5–N1–C6	-179.38(15)	-179.95(15)	175.1(2)
C5–N1–C6–C7	177.28(15)	178.76(15)	45.5(3)
CO_2/C_6	4.09(11)	9.29(19)	21.0(2)
Sn–O1			2.2182(17)
Sn–O2[i a]			2.3312(17)
O1–Sn–C14			90.88(9)
O1–Sn–C15			93.87(9)
O1–Sn–C16			94.47(9)
O2–Sn–C14			86.04(9)
O2–Sn–C15			85.91(9)
O2–Sn–C16			88.48(9)
C14–Sn–C15			117.04(12)
C14–Sn–C16			114.46(12)
C16–Sn–C16			127.58(12)

[a] Symmetry operation (i): 1-*x*, ½+*y*, ½-*z*

There are a number of closely related precedents for **LH** in the literature and these are known to exhibit significant conformational flexibility. For example, significant kinks are seen in some of the chains of the molecules, *i.e.*, about the C3–C4 bond [78.5(2)°] and C4–C5

[117.9(3)°] in the 3,5-dichlorophenyl [29] and 2-methoxyphenyl derivatives [28], respectively. Similarly, large variations are evident in the relative orientation of the chain to the attached arene ring, with the maximum twist in the C5–N1–C6–C7 torsion angle [133.95(18)°] seen in the 3,5-dichlorophenyl species [29].

The asymmetric-unit for **1** is illustrated in Fig. 2(a) and selected geometric parameters are included in Table 5. The carboxylate-C–O bonds no longer exhibit the disparity noted in the molecules of **LH**. Also contrasting the behaviour of **LH**, significant twists are noted in the backbone of the molecule, especially in the C3–C4–C5–N1 [154.5(2)°] and C5–N1–C6–C7 [45.5(3)°] torsion angles. Owing to a μ_2-bridging mode of the carboxylate residue, a one-dimensional coordination polymer is formed in the crystal and, being propagated by glide symmetry, adopts a zigzag topology, Fig. 2(b). The bridges are not quite symmetric with the Sn–O1 bond length of 2.2182(17) Å being shorter than Sn–O2^{i} of 2.3312(17) Å; symmetry operation (i): 1-*x*, ½+*y*, ½-*z*. The five-coordinate geometry for the tin atom is completed by three methyl substituents with the range of Sn–C bond lengths being narrow, indeed, experimentally equivalent, *i.e.* 2.114(3) Å [Sn–C15] to 2.126(3) Å [Sn–C14]. In terms of coordination geometry, the three methyl-C atoms occupy equatorial positions in a distorted trigonal-bipyramidal geometry. In this description, the axial O1–Sn–O2^{i} angle is 176.42(6)°. The O–Sn–O angles are close to perpendicular with those involving the more strongly bound O1 atom systematically greater than those involving the O2 atom, Table 5. While the C–Sn–C angles are close to trigonal, the C15–Sn–C16 angle is more than 10° wider than the other two angles reflecting the close (intramolecular) approach of the O2 atom; Sn···O2 = 2.9669(18) Å. A measure of the distortion from the ideal coordination geometry is the value of τ [54]. For ideal square-pyramidal and trigonal-bipyramidal geometries, τ equates to 0.0 and 1.0, respectively. In **1**, τ computes to 0.81; again the distortion from the ideal trigonal-bipyramidal geometry can be traced to the relatively close approach of the O2 atom. The crystallographic results are in accord with the values calculated from the NMR study.

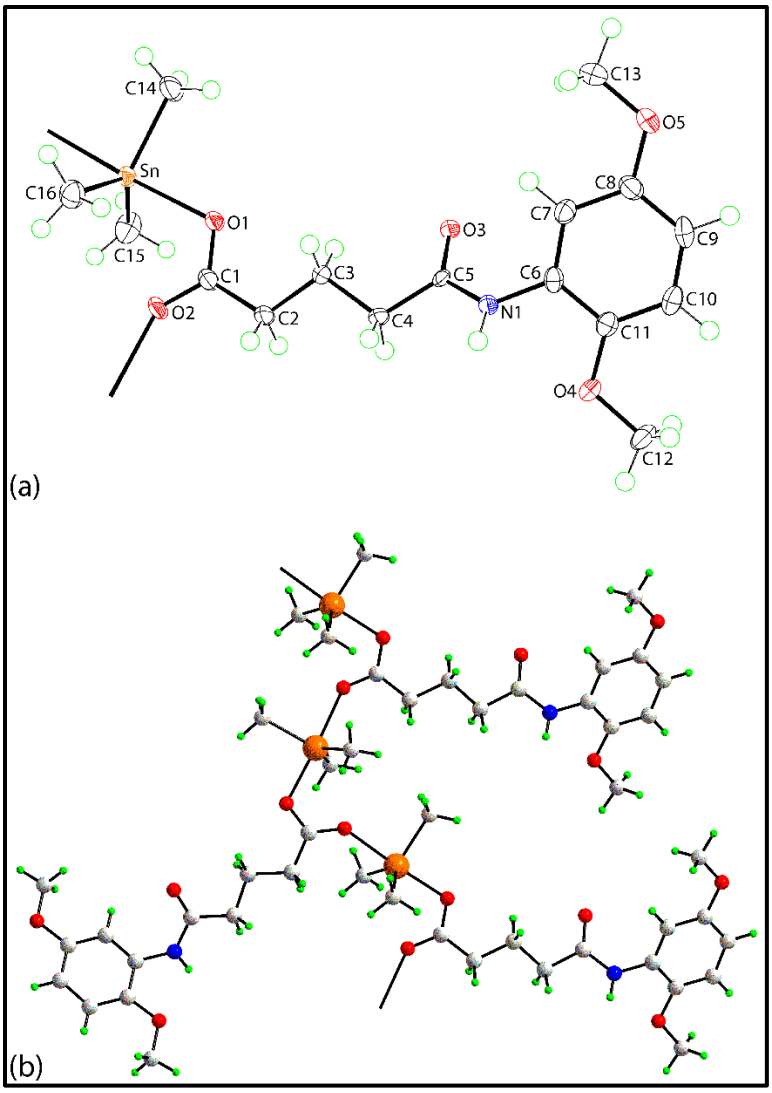

Fig. 2. (a) The asymmetric unit of **1**, showing the atom-labelling scheme and displacement ellipsoids at the 70% probability level and (b) the one-dimensional, zigzag coordination polymer constructed by μ_2-bridging by the carboxylate ligand.

Organotin carboxylates are well-studied classes of compounds and their crystal structures many and varied [55]. There are two basic structural types for triorganotin carboxylates, namely isolated and polymeric, featuring five-coordinate *cis*-R_3O_2 and *trans*-R_3O_2 donor sets, respectively, assignments depending on the relative lengths of the Sn-O bonds [55]. The adoption of one structural type over the other has been related to steric congestion exerted by the tin-bound substituents [56]. In addition, rare cyclo-tetrameric and cyclo-hexameric structural motifs are also known [55].

3.3.2 Molecular packing

Conventional hydrogen bonding interactions features prominently in the crystal of **LH**; geometric parameters characterising the intermolecular contacts in **LH** and **1** are summarised in Table 6. The amide-N–H atoms are bifurcated forming, as noted above, intramolecular amide-N–H···O(methoxy) as well as amide-N–H···O(carbonyl) hydrogen bonds; these are complimented by hydroxyl-O–H···O(amide) hydrogen bonds. The specified hydrogen bonds occur between the independent molecules, linking them into a supramolecular tape with a flat topology approximately parallel to (1 1 0) and featuring non-symmetric, 16-membered {···HOC_5NH···OC_5O} synthons, Fig. 3. The tapes are connected into a three-dimensional architecture *via* carbonyl-O···π(C6a-C11a), methylene-C–H···π(C6a-C11a) and methyl-C–H···π(C6b-C11b) as detailed in Table 6; the unit-cell diagram given in ESI† Fig. S2.

Table 6. Selected geometric parameters (Å, °) characterising intra-/inter-molecular in the crystals of **LH** and **1**

A	H	B	H…B (Å)	A…B (Å)	A–H…B (°)	Symmetry operation
LH						
N1a	H1n	O4a	2.167(18)	2.6007(19)	109.7(15)	*x*, *y*, *z*
N1b	H2n	O4b	2.172(17)	2.6027(18)	109.9(15)	*x*, *y*, *z*
N1a	H1n	O2b	2.238(15)	3.079(2)	159.3(17)	*x*, *y*, *z*
O1a	H1o	O3b	1.846(17)	2.6909(18)	176(2)	*x*, *y*, *z*
N1b	H2n	O2a	2.359(19)	3.174(2)	155.3(17)	*x*, *y*, 1+*z*
O1b	H2o	O3a	1.852(16)	2.6964(18)	172(2)	*x*, *y*, 1+*z*
C1a	O2a	Cg1	3.6210(16)	3.7394(18)	86.22(11)	1-*x*, 1-*y*, -*z*
C2a	H2a1	Cg1	2.76	3.6022(18)	143	-*x*, 1-*y*, -*z*
C12b	H12d	Cg2	2.87	3.842(2)	169	½+*x*, 1½-*y*, ½+*z*
C13b	H13d	Cg2	2.95	3.655(2)	130	-½+*x*, 1½-*y*, -½+*z*
1						
N1	H1n	O3	2.03	2.912(2)	176	1½-*x*, -½+*y*, *z*
C9	H9	O1	2.58	3.529(3)	173	½+*x*, 1½-*y*, 1-*z*

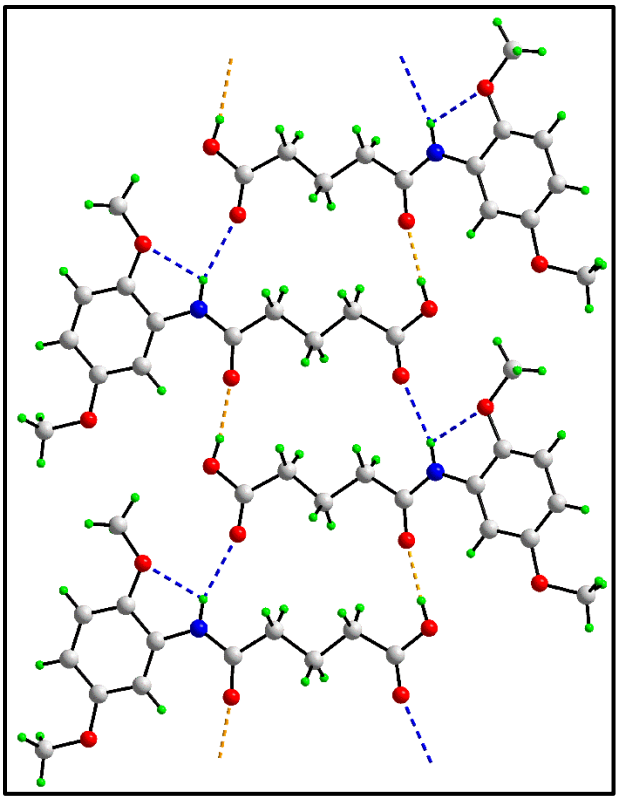

Fig. 3. The supramolecular tape in the crystal of **LH**. The amide-N–H···O(carbonyl) and hydroxyl-O–H···O(amide) hydrogen bonds are shown as blue and red dashed lines, respectively.

In the crystal of **1**, the coordination polymers are aligned along the *b*-axis. As shown in Fig. 4(a), neighbouring chains are linked by amide-N–H···O(carbonyl) hydrogen bonds along the a-axis and these lead to a two-dimensional array with a zigzag topology (glide symmetry), Fig. 4(b). The layers stack along the *c*-axis in an ···ABAB··· fashion but there are no directional interactions between them; a view of the unit-cell contents is shown in ESI† Fig. S2.

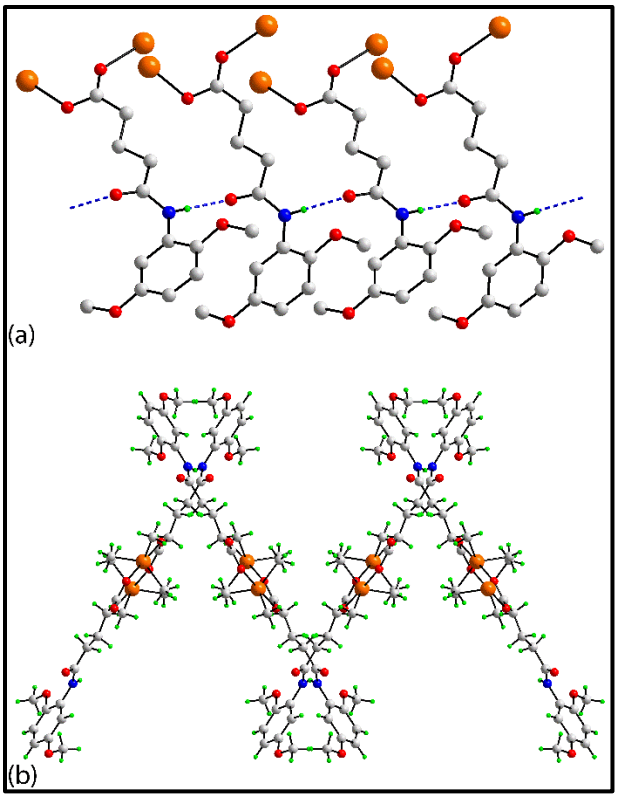

Fig. 4. Supramolecular association in the crystal of **1**: (a) chains of amide-N–H···O(carbonyl) hydrogen bonds, shown as blue dashed lines, linking two coordination polymers and (b) zigzag arrays mediated by amide-N–H···O(carbonyl) hydrogen bonds. In (a), the methyl groups and non-participating H atoms are omitted for clarity.

3.4. GM-MS analysis of LH

The ligand, **LH**, was also analysed by GC-MS (spectrum is given in ESI Figure 3 of supplementary data) using electron impact (EI) at 70 eV. The following major peaks with fragmentation were observed in the mass spectrum. $[C_{13}H_{18}NO_5]^+$: m/z = 268$(M+1)^+$, $[C_{13}H_{17}NO_5]^+$: m/z = 267$(M)^+$, $[C_{12}H_{12}NO_3]^+$: m/z = 218, $[C_8H_{12}NO_2]^+$: m/z = 154, $[C_8H_{11}NO_2]^+$: m/z = 153 $[C_8H_{10}O_2]^+$: m/z =138(100), $[C_7H_{10}O]^+$: m/z =110, $[C_2H_5O]^+$: m/z = 45.

3.5. Anti-microbial activity

CO-ADD perform the preliminary anti-microbial potential evaluation of the trial compounds **LH** and **1-3**. The anti-microbial potential of the trial compounds **LH** and **1-3** against broth solutions of key *ESKAPE* bacterial pathogens *S. aureus*, *E. coli*, *K. pneumoniae*, *A. baumannii*, and *P. aeruginosa*, as well as fungal pathogens *C. neoformans* and *C. albicans* are tested in a 384-well format in duplicate at a single concentration (32 µg/mL); perceive Table 2 for abbreviations and other information.

LH and **1**–**3** exhibited varying degrees of inhibitory activity against the five bacterial strains, Table 7. Among the screened compounds, **LH** showed the least inhibitory activity while **2** is generally the most active one. The maximum activities displayed by **1-3** are as: 97.06% against *A. baumannii* by **1**, 90.15% against *S. aureus* by **2** and 85.45% against *A. baumannii* by **3**. It is noted that the inhibition induced by **2** against *A. baumannii* was 88.88% suggesting a potential selectivity of **1-3** against this pathogen. Within the series, the most potent compound is **2** which has MIC ≤0.25 μg/mL, Table 8, against *S. aureus* and *A. baumannii*, *i.e*. lower than the MIC of the standard anti-biotics vancomycin-HCl (MIC = 1 μg/mL) and colistin-sulphate (MIC = 0.25 μg/mL), respectively.

The anti-fungal activity of the complexes, Table 7, indicates **2** has maximum activity against both *Ca* and *Cn*, even greater than that of the fluconazole against *Cn* as evidenced from the MIC value (≤0.25 μg/mL), Table 8. The pathogen-killing mechanisms of the evaluated compounds might be entirely metal-mediated, with the ligand framework just acting as a delivery vehicle for the active metal ion. It is because from the literature it was noted that metal complexes are generally better potential antibiotic drug aspirants with some important benefits over their organic ligand counter partners [20].

The MIC, CC_{50} (cytotoxicity) and HC_{10} (haemolytic activity) for each organism for **1-3** using broth microdilution method assay against the CO-ADD panel of microorganisms is given in Table 8. Majority of the metal complexes are toxic and their toxicity is not definite to bacteria but also distresses human cells. Keeping in mind the anticancer potential of the tested compounds, where cytotoxic properties are necessary, this is a concern. For this purpose, toxicity was tested against mammalian cell viability (HEK-293) and haemolytic activity against human RBC. Non-toxic compounds were defined as compounds with HEK-293 CC_{50} > 32 μg/mL and haemolytic HC_{10} > 32 μg/mL (HC_{10} is the concentration causing 10% haemolysis). The screened compounds **1-3** were marked as haemolytic. Complexes **1** and **3** were marked as non-toxic while **2** as toxic [20].

Table 7. Percentage inhibition induced by **LH** and **1-3** against bacteria and fungi at 32 μg/mL[a]

Comp.	% Inhibition							Sel	Act
	Sa	***Ec***	***Kp***	***Pa***	***Ab***	***Ca***	***Cn***		
LH	-27.02	6.84	21.26	7.71	11.68	6.81	8.52	0	0
1	21.46	40.07	28.53	16.44	97.05	2.96	-49.06	1	1
2	90.15	62.39	38.59	65.61	88.88	105	108.5	3	2
3	82.11	47.21	34.78	29.67	85.47	94.14	97.47	2	2

a) Active compound: Inhibition ≥ 80% and abs(Z-Score) > |2.5|. Partial Active: Inhibition = 50.9 – 79.9% and abs(Z-Score) < |2.5|. Inactive compounds: Inhibition < 50% and abs(Z-Score) < |2.5|

Table 8. MIC and cytotoxicity values (μg/mL) for **1-3**.

Comp.	MIC							Cytotoxicity	
	Anti-bacterial					Anti-fungal		HEK-293	RBC
	Sa	***Ec***	***Kp***	***Pa***	***Ab***	***Ca***	***Cn***	(CC_{50})	(HC_{10})
1	>32	>32	>32	>32	32	>32	>32	>32	>32
2	≤0.25	>32	>32	>32	≤0.25	≤0.25	≤0.25	≤0.25	>32
3	>32	>32	>32	>32	>32	>32	32	>32	>32
Col.[a]		0.125	0.25	0.25	0.25	-	-	-	-
Van.[a]	1	-	-	-	-	-	-	-	-
Flu.[a]	-	-	-	-	-	0.125	8	-	-

a) Abbreviations: Col: colistin-sulphate; Van: vancomycin-HCl; Flu: fluconazole

3.6. DNA interactions

The interactions between **1-3** and DNA were studied *via* UV-visible spectroscopy with the results summarised in Figs. 5-6, respectively. Each compound exhibited two strong bands at approximately 200-230 and 235-300 nm attributed to π–π* and n-π* transitions, respectively. Two phenomena were experienced upon interaction with DNA: hypochromism along with a bathochromic effect of 2-5 nm. After insertion into DNA nitrogenous base pairs, the intercalated molecule's π* orbital interacts with the base pairs' π orbital, lowering the energy of π-π* transition, causing the red/bathochromic shift. The coupling of the respective, partially filled orbitals also reduces the transition probability, resulting in the observed hypochromic shift. Intercalation, which

includes significant stacking between the chromophore and the base pairs of DNA, is the primary way of interaction when these two processes occur [40-42]. The binding constant (K_b) was determined from the intercept to slope ratio of the plot of $A_o/(A-A_o)$ *vs* 1/[DNA] as shown in the inset of Figs 5-8. The K_b value was then used to determine the Gibb's free energy value (which relates to the spontaneity of DNA-compound adduct formation) from the equation $\Delta G = -RT\ln K_b$, where the spontaneity of the DNA-compound adduct formation is evidenced by negative sign of ΔG [40-42].

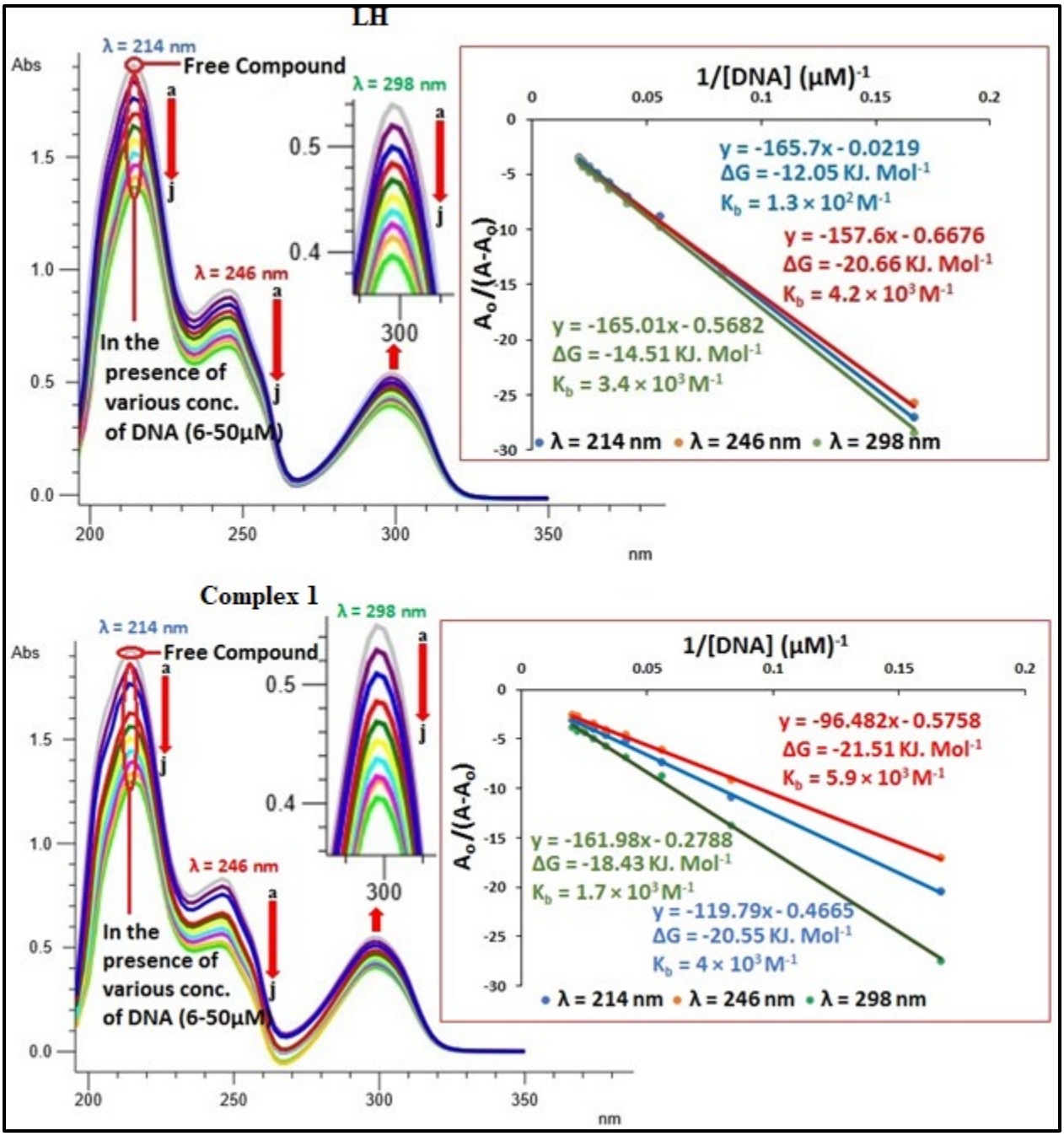

Fig. 5. DNA binding spectrum of 1 mM **LH** and complex **1**, in the absence and presence of increasing conc. of DNA as shown by arrowhead.

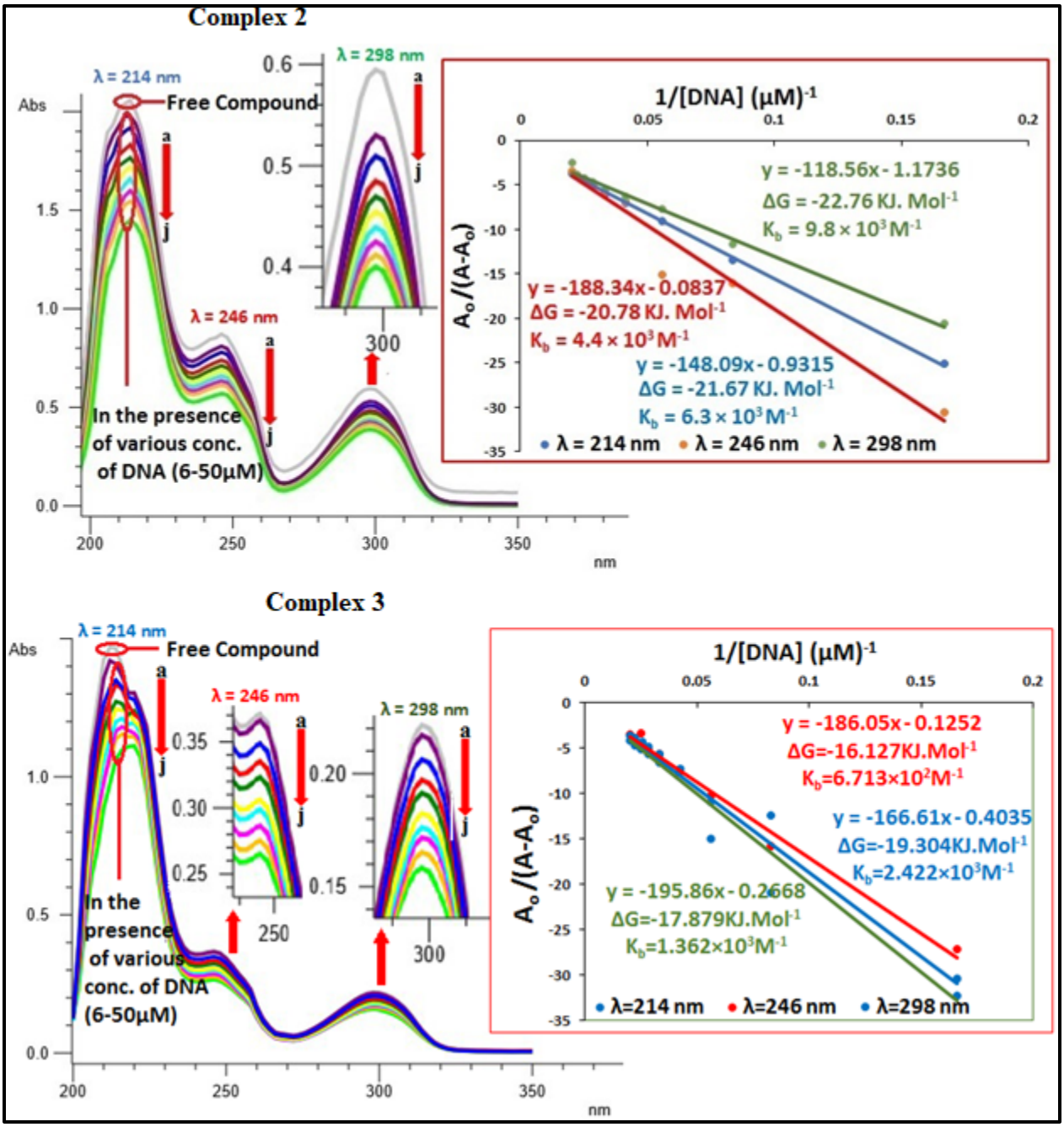

Fig. 6. DNA binding spectrum of 1 mM complexes **2** and **3**, in the absence and presence of increasing conc. of DNA as shown by arrowhead.

The viscometric approach further validated the intercalative binding mechanism between **1-3** and DNA. The viscosity of DNA in the presence of various concentrations of **1-3** was enhanced in the viscosity measurements due to the entrance of the relevant compound between the DNA bases, resulting in DNA lengthening. The intercalative binding mechanism is indicated by an

increase in the viscosity of DNA when varied concentrations are added [39]. Figure 7 shows the relationship between relative viscosity and the ratio of **1-3**/DNA concentration.

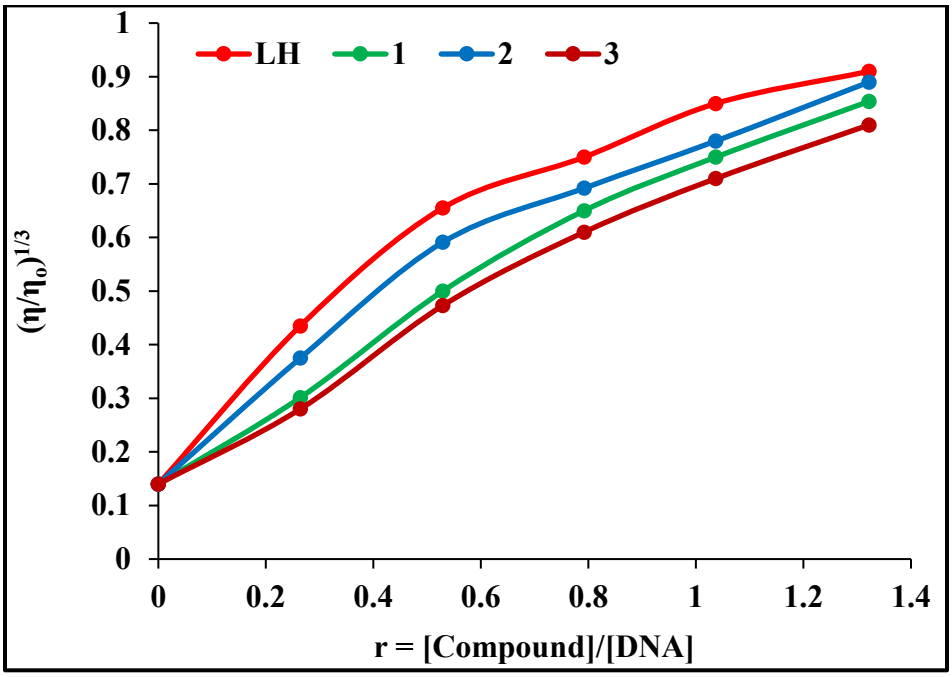

Fig. 7. Viscosity plots for the interaction of **LH** and **1-3** with DNA.

Cytotoxicity study

The main goal of the cytotoxicity study was to see how different doses of the screened compounds affected cell viability in order to see if they had anti-cancer potential. The growth inhibition experiments on MG U87 cell lines were performed using incremental dosages ranging from 12.5 to 400 µM as is shown in Fig. 8. The findings revealed that the cytotoxicity of the screened compounds is dose dependent. Thus, when the concentration of the trial compound increases, cell growth decreases; however, at different doses, distinct compounds blocked 50 or 70% of cell growth.

Interestingly, the growth inhibition assays clearly revealed **1-3** were more cytotoxic compared to **LH**, indicating the importance of the organotin centre. Among the screened compounds, the maximum growth inhibition was found for the trimethyl derivative (**1**) (IC_{50}: 148.979 µM at 50 µM dose) while the minimum growth inhibition was shown by **LH** (IC_{50}: 527.469 at 400 µM dose). Complex **1** showed about 18% cell death even at minimum dose of 6.25 µM. The next greatest activity is shown by the tributyl complex (**2**) with IC_{50}: 217.334 µM at 100 µM dose. At 50 µM its inhibition growth is about 51%. For triphenyl complex (**3**) the 50% inhibition growth was observed at 400 µM concentration with IC_{50}: 396.418 µM. Thus, on the

basis of the preliminary screening data, the synthesised organotin(IV) carboxylate derivatives are incipient as prospective candidates for additional in-depth investigation to examine their safety and efficacy [34]. The microphotographs for the ligand and its complexes **1-3** at different concentrations are shown in Fig. 9.

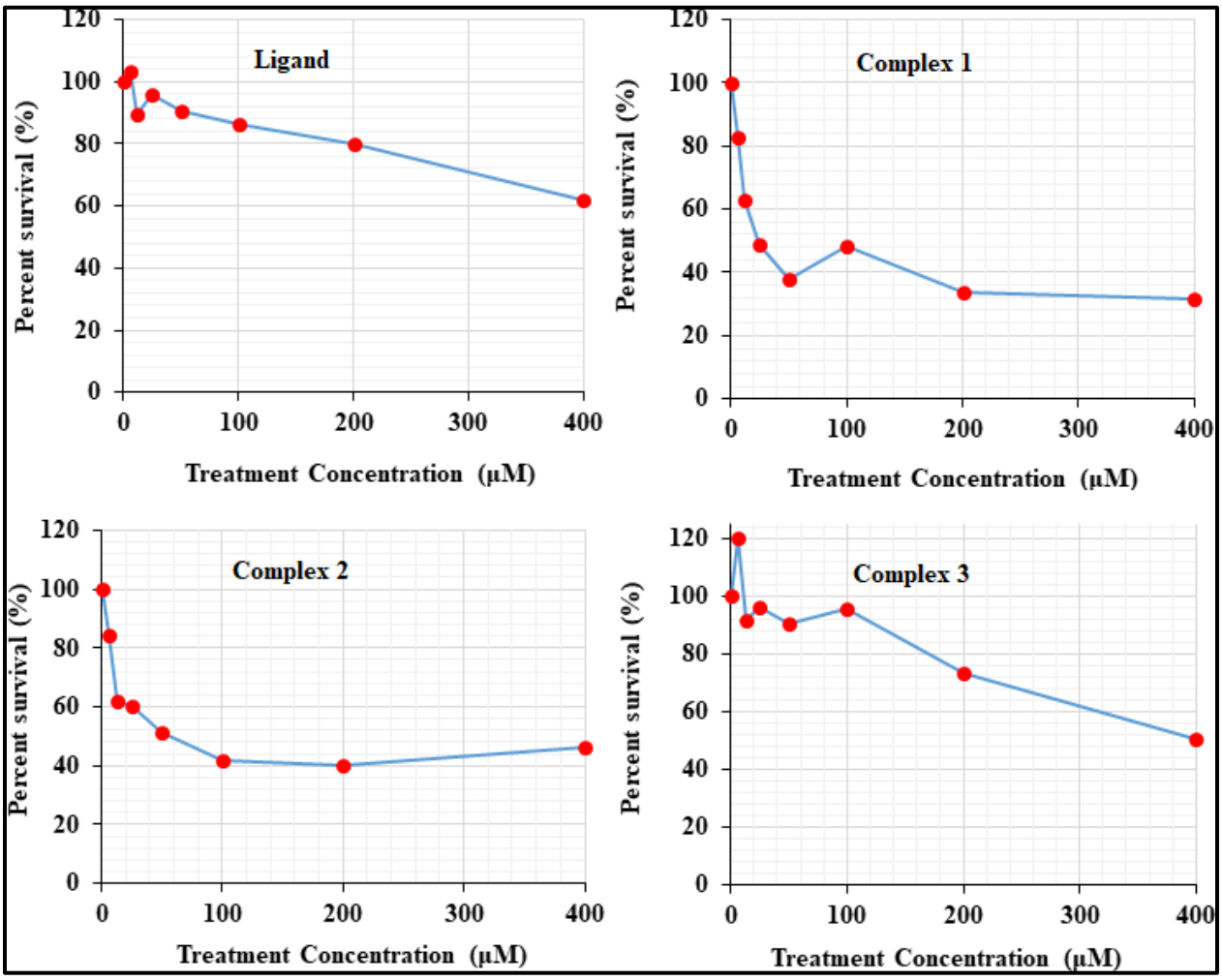

Fig. 8. Graphical representation of survival fraction of the synthesised compounds at different concentrations following 24 h of drug treatment.

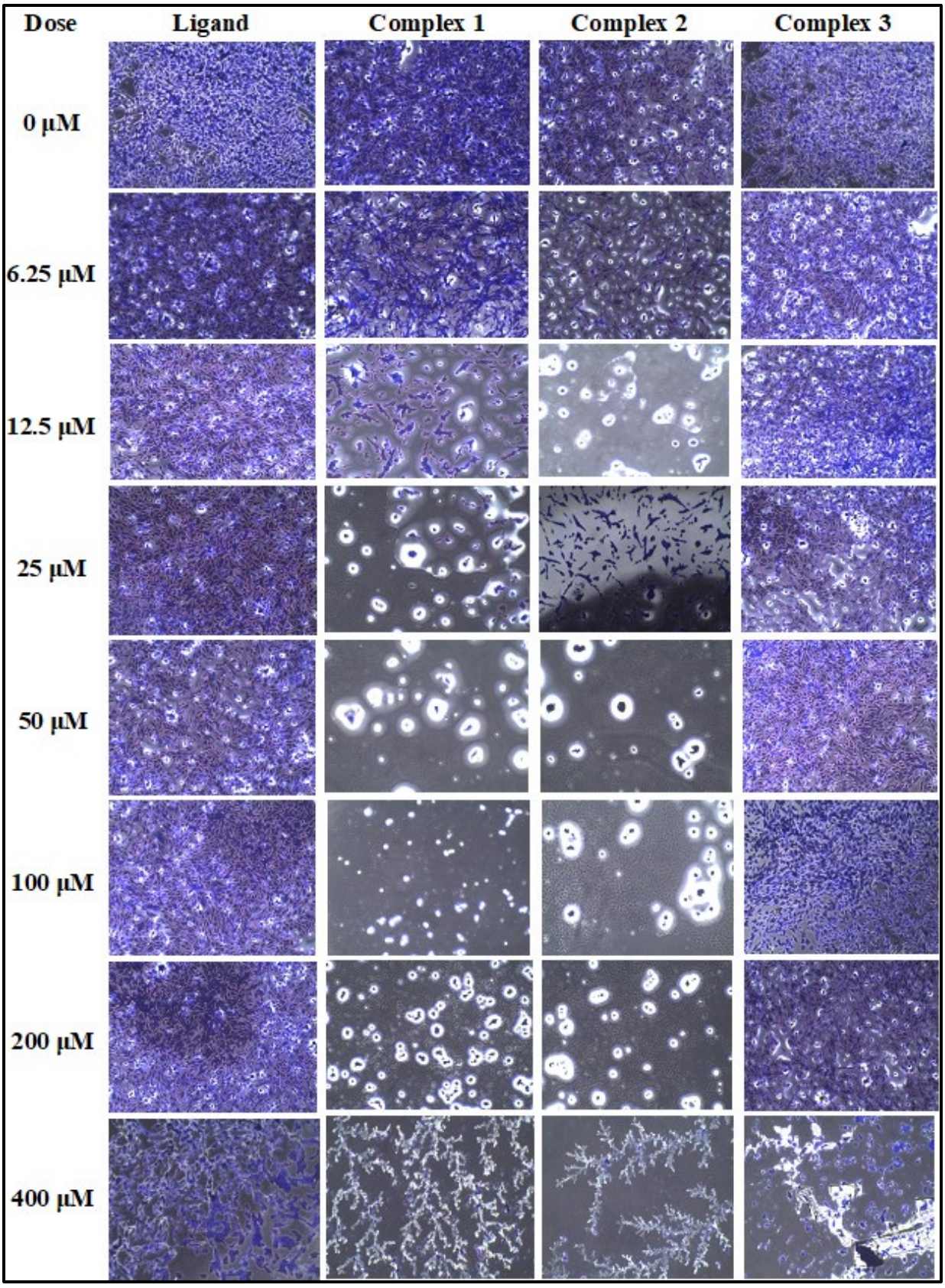

Fig. 9. Microphotographs of ligand and complexes **1-3** at different concentration

3.7. Anti-oxidant activity

The DPPH radical is the most extensively employed radical for determining a compound's reducing or anti-oxidant capability. The interaction of **LH** and **1-3** with DPPH was used to assess their anti-oxidant capacity. Compounds with anti-oxidant potential must donate an electron to the free DPPH radical (1,1-diphenyl-2-picryl-hydrazyl) to convert it to 1,1-diphenyl-2-picryl-hydrazine. The DPPH radical exhibits a deep-violet hue with a prominent absorption peak at 517 nm. When different concentrations of the chemical are added, the radical character of the DPPH alters as its unpaired electron is coupled, resulting in a reduction in absorbance and decolourisation [42]. Figure 10 depicts the effect of various concentrations of **LH** and **1-3** as well as that of ascorbic acid, which was employed as a standard. The maximum scavenging action was observed for **1** (91% at 1800 µL/mL concentration). The activity of the ascorbic acid at 1800 µL/mL concentration is 99%. The activity of the three complexes is greater than that of **LH**.

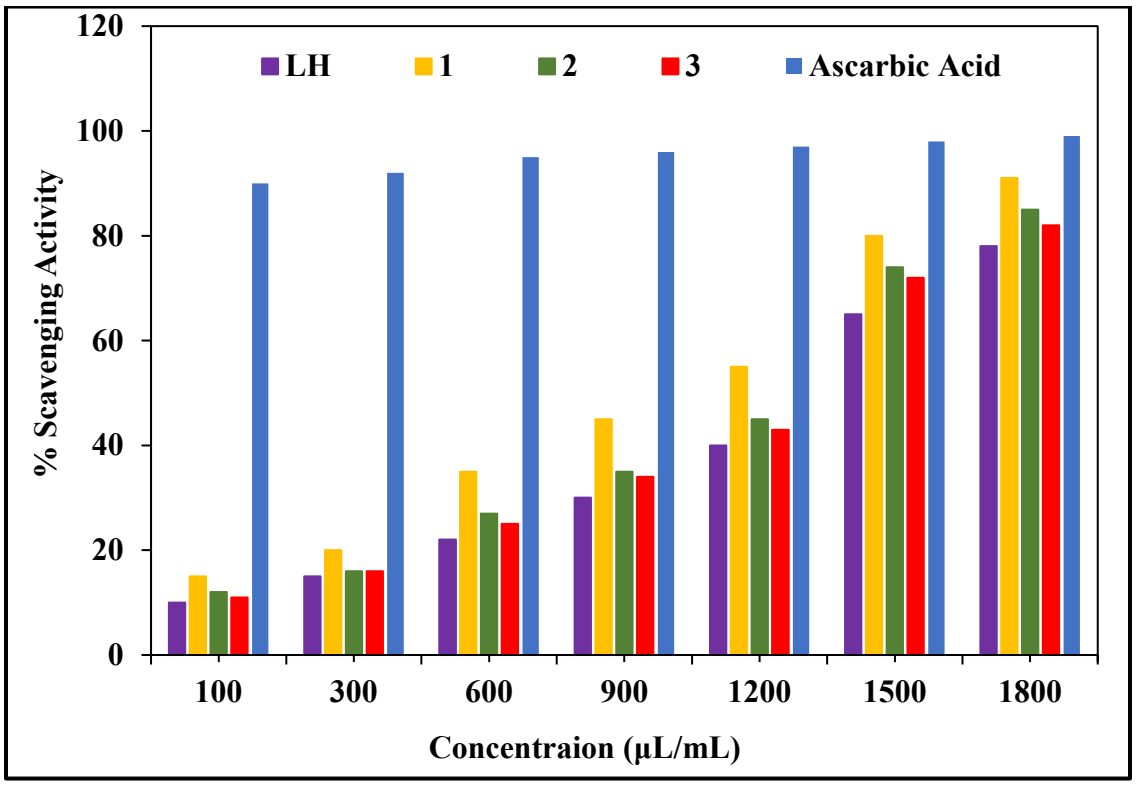

Fig. 10. DPPH scavenging activity of **LH** and complexes **1-3** using ascorbic acid as standard.

3.8. Physicochemical properties and ADME parameters

Tables 8 and 9 summarise the physicochemical features, ADME parameters and drug-likeness rule violations of the examined compounds. The mol. Wt (MW), topological polar surface area (tPSA), molar refractivity, percentage of sp^3 carbon atoms (Fsp^3) and various H-bond characteristics are all analysed physicochemical attributes. In the literature, there are numerous filter approaches that provide a set of guidelines for evaluating drug-likeness profiles of compounds. The following are the filters and rules covered in this work:

i. Lipinski (Pfizer) filter [57]
ii. Ghose filter [58]
iii. Veber (GSK) filter [59]
iv. Egan (Pharmacia) filter [60]
v. Muegge (Bayer) filter [61]

An orally active medicine should not break the aforementioned conditions more than once, according to the filters. tPSA is the total of the surface areas of polar atoms in a molecule and it is used to calculate drug transport parameters. Low tPSA values in molecules indicate a stronger propensity for transport. **LH** (84.86 Å²) and **1-3** (73.86 Å²) have tPSA values that are within the range of values recommended by different drug-likeness filters. Fsp^3 is a recent parameter [62] that is used to measure drug-likeness qualities of compounds, with values of 0.38 for **LH** and 0.50, 0.68 and 0.16 for **1-3**, respectively. The suggested molar refractivity range for a molecule is between 40 and 130. The values for **LH** and **1** are within this range but not **2** and **3**. Lipophilicity is an important characteristic that influences medication action in humans. The most commonly used measure of lipophilicity is the logP value, which is an indicator of a drug's permeability to reach its target tissue in the body. Table 9 shows the logP values employed by the various drug-likeness filters (MLogP for Lipinski [57], WLogP for Ghose [58] and Egan filters [59], XLogP for Muegge filter [60] as well as their mean values (consensus logP). All logP values for **LH** and **1-3** are in accordance with general guidelines (<5). ESOL is aqueous-solubility parameter of molecules proposed by Delenay [63] and is considered one of the key physical properties in drug discovery. Table 8 shows that **LH** and c**1** have ESOL values in the soluble class, while **2** and **3** have ESOL values in the poorly-soluble class.

The bioavailability score (BS) estimates the likelihood of a molecule having oral bioavailability in rats or demonstrable Caco-2 permeability, with a bioavailability score value of

> 0.1068 predicted for a compound in rats. Poor bioavailability reduces molecular activity and increases inter-individual variability, resulting in an unanticipated pharmacological response [64]. For **LH** and **1-3**, the bioavailability scores, Table 9, are all greater than the threshold value.

Potts *et al*. [65] proposed the log(Kp) skin permeation parameter; a high negative log(Kp) value of a molecule implies that it has less penetration into the skin. For **LH** and **1-3**, the log(Kp) values are all negative (Table 8).

In summary, Tables 8 and 9 show the physicochemical properties, lipophilicity and water-solubility values for **1-3** used by various drug filters. Moreover, the favourable bioavailability scores (BS), drug score (DS) and the higher skin absorption indicate that these compounds can be potential drug candidates. Compounds **1-3** are non-mutagenic, non-tumorigenic, non-irritant and have no reproductive effect.

Figure 11 show a radar image of the screened compounds. Using six different physicochemical criteria, the resultant radar image indicates chemicals in the pink area that can be termed drug-like. Lipophilicity (LIPO), molecular size (SIZE), polarity (POLAR), solubility (INSOLU), flexibility (FLEX) and saturation are the terms used to describe these characteristics (INSATU). According to five distinct criteria, the radar image for **LH** totally falls within the pink area, while **1-3** are slightly outside the pink range.

Figure 12 describes the BOILED-Egg model for **LH** and **1-3**. The yellow area of the BOILED-Egg model symbolises the bridging of the blood-brain barrier, while the white area reflects gastrointestinal absorption. In this model, TPSA value on x-axis is plotted *vs*. WLOGP value on y-axis. The red dot symbolises the chosen molecule, and the status of this point in the yellow, white and grey areas is used to infer pharmacokinetic features. As shown in Fig. 12, **LH** and **2** are anticipated not to be candidates as drug molecules due to their absorption status in the blood-brain barrier, whereas **1** and **3** are predicted to be candidates according to the same criterion. The transit of a drug candidate molecule into the lymph and blood circulation, on the other hand, is influenced by a variety of circumstances. The size of the molecule, its MW (mol. Wt.) and its hydrophilic and lipophilic structure are some of these parameters.

Table 8. Physicochemical properties, lipophilicity, solubility and toxicity risks for **LH** and **1**-**3**.

Property	LH	1	2	3
Physicochemical Properties				
M. Wt (g/mol)	257.28	430.07	556.31	616.28
Fsp^3	0.38	0.50	0.68	0.16
No. rotatable bonds	8	6	19	13
No. H-bond acceptors/donor	5/2	5/1	5/1	5/1
Molar refractivity	69.93	91.73	135	152.37
tPSA (Å²)	84.86	73.86	73.86	73.86
Lipophilicity				
log($P_{o/w}$) (iLOGP)	2.22	0.00	0.00	0.00
log($P_{o/w}$) (XLOGP)	1.53	2.58	6.86	6.46
log($P_{o/w}$) (WLOGP)	1.71	3.00	6.51	3.83
log($P_{o/w}$) (MLOGP)	0.88	1.65	3.67	4.18
log($P_{o/w}$) (SILICOS-IT)	1.56	2.04	5.81	5.41
Consensus log($P_{o/w}$)	1.58	1.85	4.57	3.98
Water-solubility				
log(*S*) (ESOL)	-2.17	-3.66	-6.50	-7.34
Solubility (mg/mL)	1.82	9.30e-02	1.78e-04	2.82e-05
Class	S	S	PS	PS
Toxicity Risks				
Mut.	*	***	***	***
Tum.	*	***	***	***
Irr.	*	**	***	**
RE	*	**	**	**

S: Soluble; PS: Poorly Soluble; RE: Reproductive effect; Irr: Irritant; Tum: Tumorigenic; Mut: Mutagenic; *: Not toxic; **: Moderately toxic; ***: Highly toxic

Table 9. Drug-likeness, pharmacokinetics and medicinal chemistry for **LH** and **1-3**[$]**.**

Property	LH	1	2	3
Drug-likeness				
Lipinski	√; 0 viol.	√; 0 viol.	√; 0 viol.	no; 2 viol.: MW>500, MLOGP>4.15
Ghose	√	√	√	no; 2 viol.: MW>480, MR>130
Veber	√	√	√	no; 1 viol.: Rotors>10
Egan	√	√	√	yes
Muegge	√	√	√	no; 2 viol.: MW>600, XLOGP3>5
BS	0.56	0.55	0.85	0.17
DS	0.48	0.1	0.26	0.06
Pharmacokinetics				
GA	high	high	high	high
BBB permeant	no	√	no	√
PGS	no	√	√	√
Cyto. P450 1A2 I	no	no	no	no
Cyto. P450 2C19 I	no	no	no	no
Cyto. P450 2C9 I	no	no	no	no
Cyto. P450 2D6 I	no	no	no	√
Cyto. P450 3A4 I	no	no	√	no
SP (logKp, cm/s)	-6.84	-7.09	-4.82	-5.47
Medicinal Chemistry				
PAINS	☼	☼	☼	☼
Brenk	☼	☼	☼	☼
LL	no; 1 viol.: Rotors > 7	no; 2 viol.: MW > 350, Rotors > 7	No; 3 viol.: MW > 350, Rotors > 7, XLOGP3 > 3.5	No; 3 viol.: MW > 350, Rotors > 7, XLOGP3 > 3.5
SA	2.04	2.84	4.37	4.70

$Viol: violation; GA: Gatrointestinal absorption; SA: Synthetic accessibility; SP: Skin permeation; LL: Lead-likeness, DS: Drug Score; Cyto: Cytochrome; I: Inhibitor; PGS: P-glycoprotein substrate; √: yes; ☼: 0 alert

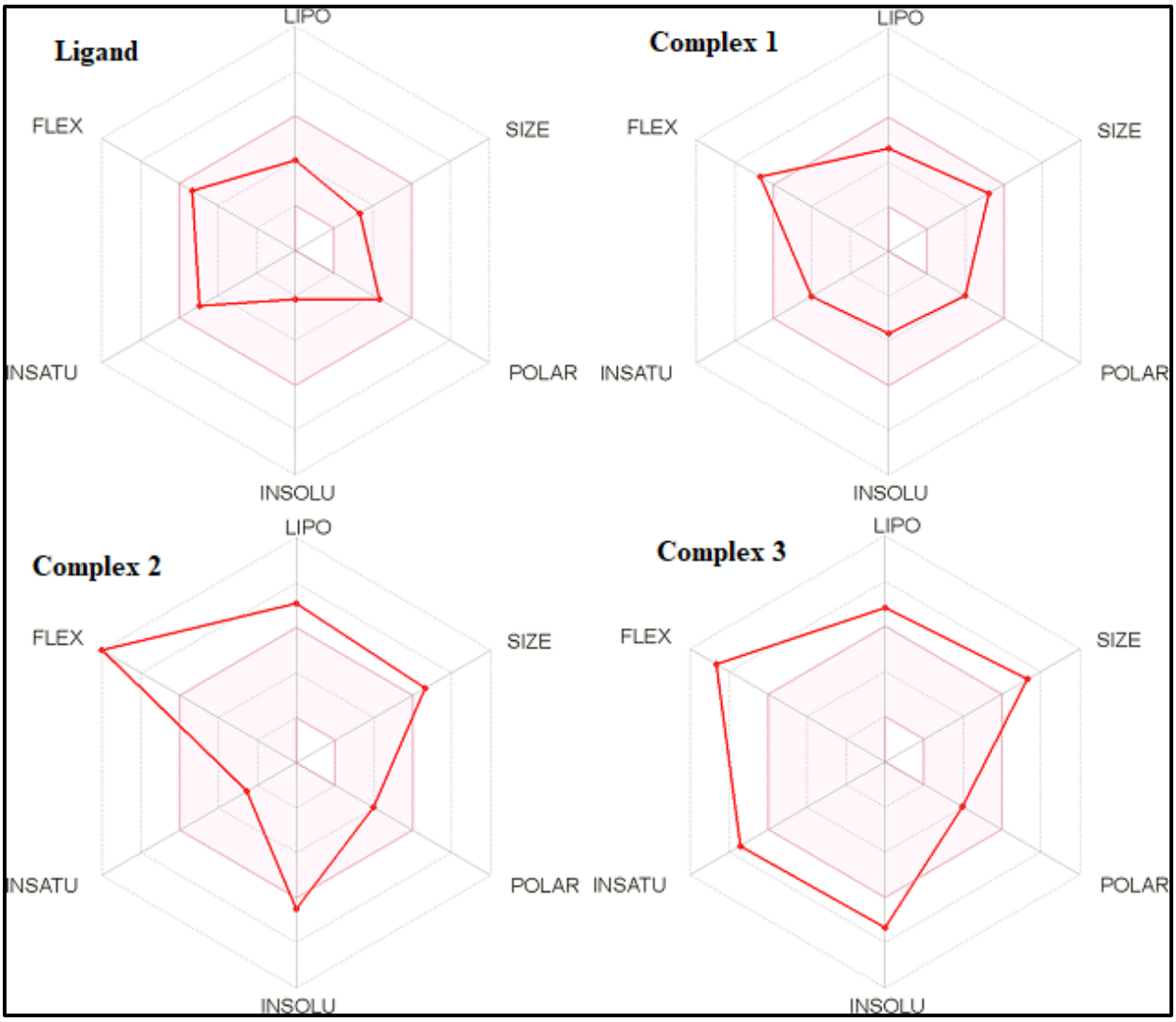

Fig. 11. Radar images for **LH** and **1-3**.

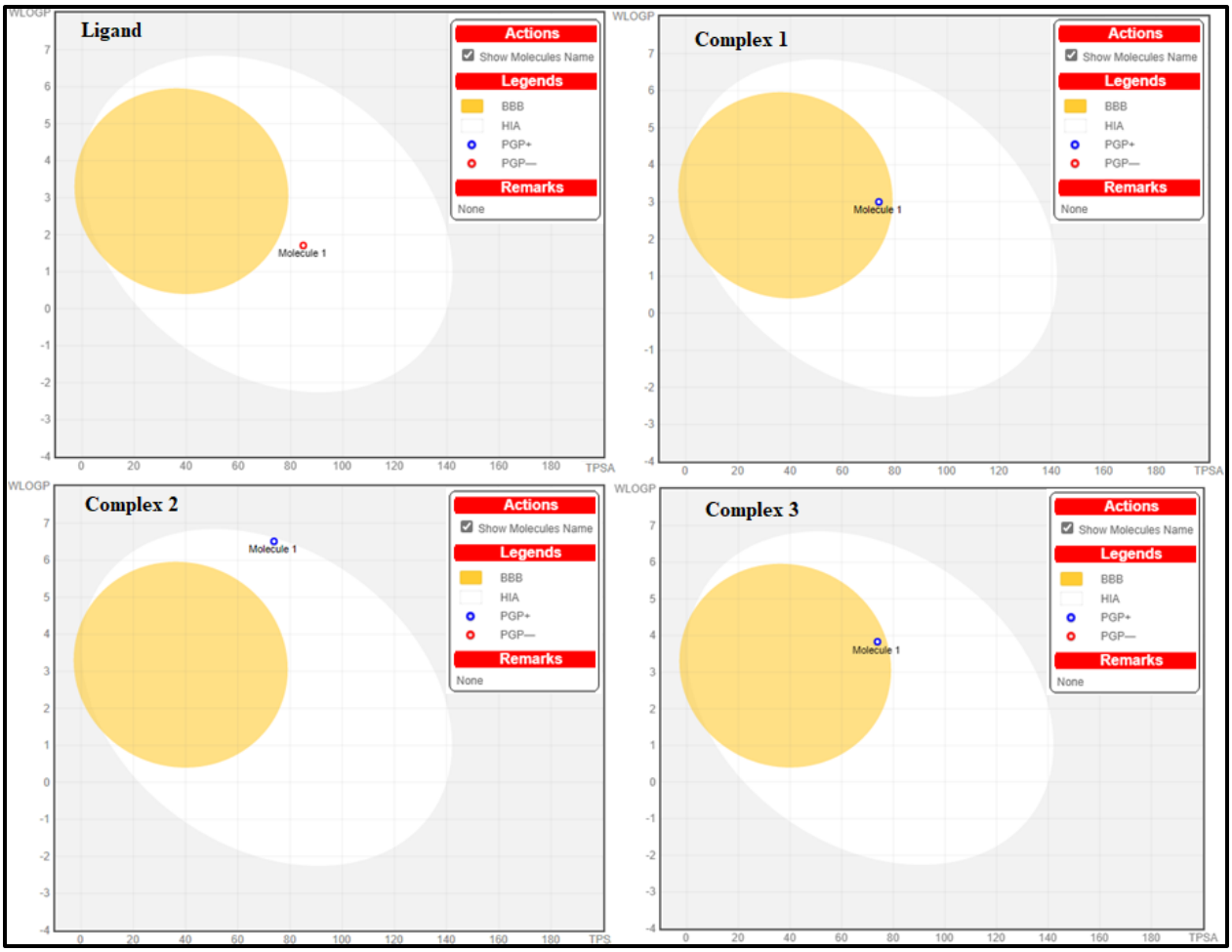

Fig. 12. BOILED-Egg model for **LH** and **1-3**.

Conclusions

Three new triorganotin carboxylates, R_3SnL, for R = Me, *n*-Bu and Ph; L = 4-[(2,5-dimethoxyphenyl)carbamoyl]butanoate, are reported. Crystallography on Me_3SnL indicates a 1D coordination polymer in the solid-state. The strong stacking relationship between the aromatic chromophore and base pairs of DNA is responsible for the intercalation mode of interaction with DNA. The intercalative binding mode was further supported by the increase in viscosity of DNA during the interaction with compound. The anti-microbial activity of some of the synthesised performed against five bacterial and two fungal strains fall in the category of active compounds, indicating their potential as drug candidates against both bacteria and fungi. The cytotoxicity (CC_{50}) of complex **2** against the human embryonic kidney cells (HEK-293) highlights its potential against the cancerous cell lines. A maximum of 91% DPPH scavenging at 1800 µL/mL

concentration was shown by the **1**. *In silico* studies suggest these compounds possess high gastrointestinal absorption and blood brain brayer (BBB) permeability properties. Similarly, good bioavailability scores (0.85), drug score (0.44) and the higher skin absorption indicate that these compounds can be potential drug candidates.

Acknowledgement

M. Sirajuddin and B. Hanifa are thankful to the Higher Education Commission (HEC) Pakistan for financial support under NRPU Grant # 20-17572/NRPU/R&D/HEC/2021. The anti-microbial activity was checked by CO-ADD, funded by the Welcome Trust (UK) and The University of Queensland (Australia). The authors also gratefully acknowledge Sunway University Sdn Bhd (Grant no. GRTIN-IRG-01-2021) for support of crystallographic studies.

CCDC reference

Crystallographic data for the structure reported in this paper has been deposited with the Cambridge Crystallographic Data Centre, CCDC 2130960 and 2130961 for **LH** and Complex **1**, respectively. Copies of this information may be obtained free of charge from The Director, CCDC, 12, Union Road, Cambridge CB2 1EZ. Fax: +44 1223 336 033 or e-mail deposit@ccdc.cam.ac.uk or http://www.ccdc.cam.ac.uk.

Footnote

† Electronic supplementary information (ESI) available: Unit-cell diagrams for **LH** and **1**.

References

[1] M. Sirajuddin, N. Uddin, S. Ali, V. McKee, S. Z. Khan and K. Malook, Synthesis, spectroscopic characterization, crystal structure, DNA interaction study and *in vitro* biological screenings of 4-(5-chloro-2-hydroxyphenylamino)-4-oxobut-2-enoic acid, Spectrochim. Acta Part A Mol. Biomol., 134 (2015) 244–250.

[2] M. Sirajuddin, S. Ali, A. Shahnawaz, F. Perveen, S. Andleeb and S. Ali, Exploration of Biological Potency of Carboxylic Acid Derivatives: Designing, Synthesis, Characterizations and Molecular Docking Study, J. Mol. Struct., 1207 (2020) 127809.

[3] O. Ivasenko and D. F. Perepichka, Mastering fundamentals of supramolecular design with carboxylic acids. Common lessons from X-ray crystallography and scanning tunneling microscopy, Chem. Soc. Rev., 40 (2011) 191–206.

[4] P. Tundo, M. Musolino and F. Aricò, The reactions of dimethyl carbonate and its derivatives, Green Chem., 20 (2018) 28–85.

[5] M. Tahir, M. Sirajuddin, M. Zubair, A. Haider, A. Nadman, S. Ali, F. Perveen, H. B. Tanveer and M. N. Tahir, Designing, spectroscopic and structural characterization and evaluation of biological potential as well as molecular docking studies of Zn(II) based metallo pharmaceuticals, J. Iran. Chem. Soc., (2021) 1–14.

[6] L. Pellerito and L. Nagy, Organotin (IV)$^{n+}$ complexes formed with biologically active ligands: equilibrium and structural studies, and some biological aspects, Coord. Chem. Rev., 224 (2002) 111–150.

[7] A. Ahmed, G. A. El-Hiti, A. G. Hadi, D. S. Ahmed, M. A. Baashen, H. Hashim and E. Yousif, Photostabilization of poly (vinyl chloride) films blended with organotin complexes of mefenamic acid for outdoor applications, Appl. Sci., 11 (2021) 2853.

[8] S. E. H. Etaiw, H. Marie, E. M. Shalaby, R. S. Farag and F. A. Elsharqawy, Sensing and photocatalytic properties of nanosized Cu (I) CN organotin supramolecular coordination polymer based on pyrazine, Appl. Organomet. Chem., 33 (2019) e5114.

[9] M. Sirajuddin, M. Tariq and S. Ali, Organotin(IV) carboxylates as an effective catalyst for the conversion of corn oil into biodiesel, J. Organomet. Chem., 779 (2015) 30–38.

[10] M. Sirajuddin, S. Ali, A. Haider, N. A. Shah, A. Shah and M. R. Khan, Synthesis, characterization, biological screenings and interaction with calf thymus DNA as well as electrochemical studies of adducts formed by azomethine [2-((3,5-

dimethylphenylimino)methyl)phenol] and organotin(IV) Chlorides, Polyhedron, 40 (2012) 19–31.

[11] M. Tariq, S. Ali, N. Muhammad, N. A. Shah, M. Sirajuddin, M. N. Tahir, N. Khalid and M. R. Khan, Biological screening, DNA interaction studies and catalytic activity of organotin(IV) 2-(4-ethylbenzylidene) butanoic acid derivatives: Synthesis, spectroscopic characterization and X-ray structure, J. Coord. Chem., 67 (2014) 323–340.

[12] F. Shaheen, M. Sirajuddin, S. Ali, P. J. Dyson, A. Haider, M. N. Tahir and K. Shahid, Synthesis, structural elucidation and biological activities of organotin(IV) derivatives of 4-(2-thienyl)butyric acid, J. Iran. Chem. Soc., 14 (2017) 387–394.

[13] S. E. H. Etaiw, T. A. Fayed, M. M. El-bendary and H. Mari, Three-dimensional coordination polymers based on trimethyltin cation with nicotinic and isonicotinic acids as anticancer agents, Appl. Organomet. Chem., 32, (2018) e4066.

[14] M. Sirajuddin, S. Ali, V. McKee, M. Sohail and H. Pasha, Potentially bioactive organotin(IV) Compounds: Synthesis, characterization, *in vitro* bioactivities and interaction with SS-DNA, Eur. J. Med. Chem., 84 (2014) 343–363.

[15] L. H. Hurley, DNA and its associated processes as targets for cancer therapy, Nat. Rev. Canc., 2 (2002) 188–200.

[16] S. K. Shukla, V. K. Tiwari, R. Sushma and I. C. Tewari, Antimicrobial, antitumor and gastroprotective studies of some new water soluble organic derivatives of bismuth, J. Med. Chem. Lett. 1 (2011) 10–19.

[17] M. Sirajuddin, S. Ali, V. McKee and H. Ullah, Synthesis, spectroscopic characterization and *in vitro* antimicrobial, antileishmanial and anticancer activities as well interaction with Salomon sperm DNA of newly synthesized carboxylate derivative, 4-(4-methoxy-2-nitrophenylamino)-4-oxobutanoic acid, Spectrochim. Acta Part A Mol. Biomol. Spectrosc., 138 (2015) 569–578.

[18] M. Sirajuddin, V. McKee, M. Tariq and S. Ali, Newly designed organotin(IV) carboxylates with peptide linkage: Synthesis, structural elucidation, physicochemical characterizations and pharmacological investigations, Eur. J. Med. Chem., 143 (2018) 1903–1918.

[19] M. Sirajuddin and S. Ali, Organotin(IV) carboxylates as a promising potential drug candidates in the field of cancer chemotherapy, Curr. Pharm. Des., 22 (2016) 6665–81.

[20] A. Frei, J. Zuegg, A. G. Elliott, M. Baker, S. Braese, C. Brown, F. Chen, C. G. Dowson, G. Dujardin, N. Jung, A. P. King, A. M. Mansour, M. Massi, J. Moat, H. A. Mohamed, A. K. Renfrew, P. J. Rutledge, P. J. Sadler, M. H. Todd, C. E. Willans, J. J. Wilson, M. A. Cooper and M. A. T. Blaskovich, Chem. Sci., 11 (2020) 2627–2639.

[21] CrysAlis PRO, Rigaku Oxford Diffraction, Yarnton, Oxfordshire, England. 2020.

[22] G. M. Sheldrick, A short history of SHELX, Acta Crystallogr., A71 (2014) 3–8.

[23] G. M. Sheldrick, Acta Crystallogr., C71 (2014) 3–8.

[24] L. J. Farrugia, WinGX and ORTEP for Windows: an update, J. Appl. Crystallogr., 45 (2012) 849–854.

[25] DIAMOND, Visual Crystal Structure Information System, Version 3.1, CRYSTAL IMPACT, Postfach 1251, D-530 02 Bonn, Germany, 2006.

[26] A. L. Spek, checkCIF validation ALERTS: what they mean and how to respond, Acta Crystallogr., E76 (2020) 1–11.

[27] B. Hanifa, M. Sirajuddin, K. M. Lo and E. R. T. Tiekink, Crystal structure of 4-[(4-methoxy-2-nitrophenyl)carbamoyl]butanoic acid, C12H14N2O6, Z. Kristallogr. - New Cryst. Struct., 235 (2020) 1435–1437.

[28] B. Hanifa, M. Sirajuddin, H. Khan, K. M. Lo and E. R. T. Tiekink, Crystal structure of 4-[(2-methoxyphenyl)carbamoyl]butanoic acid, C12H15NO4, Z. Kristallogr. - New Cryst. Struct., 235 (2020) 1481–1483.

[29] B. Hanifa, M. Sirajuddin, K. M. Lo and E. R. T. Tiekink, Crystal structure of 4-[(3,5-dichlorophenyl) carbamoyl]butanoic acid, C11H11Cl2NO3, Z. Kristallogr. - New Cryst. Struct., 235 (2020) 1495–1497.

[30] M. Sirajuddin, B. Hanifa, S. Ullah, H. Khan, K. M. Lo and E. R.T. Tiekink, Crystal structure of 4-[(3-methoxyphenyl) carbamoyl]butanoic acid, C12H15NO4, Z. Kristallogr. – New Cryst. Struct., 235 (2020) 1519–1521.

[31] B. Hanifa, M. Sirajuddin, A. Bari, S.M. Lee, K. M. Lo and E. R. T. Tiekink, 4-[(4-Chlorophenyl)carbamoyl]butanoic acid, Molbank, 2021 (2021) M1209.

[32] B. Hanifa, M. Sirajuddin, Z. Ullah, S. Mahboob, A. Bari, S. M. Lee, K. M. Lo and E. R. T. Tiekink, 4-[(2,4-Dichlorophenyl)carbamoyl]butanoic acid, Molbank, 2021 (2021) M1227.

[33] a) M. A. T. Blaskovich, J. Zuegg, A. G. Elliott, and M. A. Cooper, Helping chemists discover new antibiotics, ACS Infect. Dis. 1 (2015) 285–287; b) K. A. Hansford, M. A. T.

Blaskovich and M. A. Cooper, Chemical philanthropy: a path forward for antibiotic discovery? Fut. Med. Chem., 8 (2016) 925–929.

[34] A. Nemat, I. N. Khan, S. Kalsoom, S. A. Malik, S. Ayub, F. Adnan, M. A. Kamal and M. Iqbal, Synthesis, anticancer evaluation and molecular docking studies of methotrexate's novel Schiff base derivatives against malignant glioma cell lines, J. Biomol. Struct. Dyn., (2020) 1–13.

[35] M. Tahir, M. Sirajuddin, A. Haider, S. Ali, A. Nadhman and C. Rizzoli, Synthesis, Spectroscopic Characterization, Crystal Structure, Interaction with DNA, CTAB as well as Evaluation of Biological Potency, Docking and Molecular Dynamics Studies of N-(3,4,5-trimethoxybenzylidene)-2, 3-dimethylbenzenamine, J. Mol. Struct., 1178 (2019) 29–38.

[36] M. Zubair, M. Sirajuddin, K. Ullah, A. Haider, F. Perveen, I. Hussain, S. Ali and M. N. Tahir, Synthesis, structural peculiarities, theoretical study and biological evaluation of newly designed O-Vanillin based azomethines, J. Mol. Struct., 1205 (2020) 127574.

[37] I. Aziz, M. Sirajuddin, A. Munir, S. Tirmizi, S. Nadeem, M. N. Tahir and W. Sajjad, Synthesis, characterization, DNA interaction study, antibacterial and anticancer activities of new Palladium(II) phosphine complexes, Russ. J. Gen. Chem., 88 (2018) 551–559.

[38] S. Noureen, M. Sirajuddin, S. Ali, F. Shaheen and M. N. Tahir, Synthesis, structural elucidation and DNA binding study of fluorine substituted organotin(IV) dithiocarbamates, Polyhedron, 102 (2015) 750–758.

[39] A. Munir, M. Sirajuddin, M. Zubair, A. Haider, S.A. Tirmizi, S. Ali, H. Khan, K. Ullah and I. Aziz, Synthesis, spectroscopic characterization and biological screenings of levofloxacin based organotin(IV) derivatives, Russ. J. Gen. Chem., 87 (2017) 2380–2390.

[40] M. Sirajuddin, S. Ali and A. Badshah, Drug-DNA interactions and their study by UV-visible, Fluorescence spectroscopies and cyclic voltammetry, J. Photochem. Photobio. B: Bio., 124 (2013) 1–19.

[41] M. Sirajuddin, S. Ali, N. A. Shah, M. R. Khan and M. N. Tahir, Synthesis, characterization, biological screenings and interaction with calf thymus DNA of a novel azomethine 3-((3,5-dimethylphenylimino)methyl)benzene-1,2-diol, Spectrochim. Acta Part A Mol. Biomol. Spectrosc., 94 (2012) 134–142.

[42] M. Sirajuddin, N. Uddin, S. Ali and M. N. Tahir, Potential bioactive Schiff base compounds: synthesis, characterization, X-ray structures, biological screenings and

interaction with salmon sperm DNA, Spectrochim. Acta Part A Mol. Biomol. Spectrosc., 116 (2013) 111–121.

[43] A. Daina, O. Michielin and V. Zoete, iLOGP: A Simple, Robust, and Efficient Description of n-Octanol/Water Partition Coefficient for Drug Design Using the GB/SA Approach, J. Chem. Inf. Model, 54 (2014) 3284–3301.

[44] A. Daina, O. Michielin and V. Zoete, SwissADME: a free web tool to evaluate pharmacokinetics, drug-likeness and medicinal chemistry friendliness of small molecules, Sci. Rep., 7 (2017) 1-3.

[45] A. Daina and V. Zoete, A boiled-egg to predict gastrointestinal absorption and brain penetration of small molecules, Chem. Med. Chem., 11 (2016) 1117–1121.

[46] M. E. Sánchez-Vergara, L. Hamui, E. Gómez, G.M. Chans and J. M. Galván-Hidalgo, Design of Promising Heptacoordinated Organotin (IV) Complexes-PEDOT: PSS-Based Composite for New-Generation Optoelectronic Devices Applications, Polymers, 13 (2021) 1023.

[47] M. Dahmani, T. Harit, A. Et-Touhami, A. Yahyi, D. Eddike, M. Tillard and R. Benabbes, Two novel macrocyclic organotin (IV) carboxylates based on bipyrazoledicarboxylic acid derivatives: syntheses, crystal structures and antifungal activities, J. Organomet. Chem., (2021) 121913.

[48] P. N. Nelson and R. A. Taylor, Theories and experimental investigations of the structural and thermotropic mesomorphic phase behaviors of metal carboxylates, J. Appl. Petrochem. Res., 4 (2014) 253–285.

[49] M. Sirajuddin, S. Ali and M. N. Tahir, Organotin(IV) derivatives based on 2-((2-methoxyphenyl)carbamoyl)benzoic acid: Synthesis, spectroscopic characterization, assessment of antibacterial, DNA interaction, anticancer and antileishmanial potentials, J. Mol. Struct., 1229 (2021) 1229, 129600.

[50] M. M. El-bendary and S. E. H. Etaiw, Structure and applications of organotin complex based on trimethyltin cation and quinaldic acid, Appl. Organometal. Chem., 32 (2018) e4152.

[51] T. P. Lockhart, W. F. Manders and E. M. Holt, Solution and solid-state molecular structures of Me2Sn(OAc)2 and its hydrolyzate, ([Me2Sn(OAc)]2O)2, by solution and solid-state

carbon-13 NMR. X-ray diffraction study of the hydrolyzate, J. Am. Chem. Soc., 108 (1986) 6611–6616.

[52] B. Wrackmeyer, Annu. Rep. NMR Spectrosc., 38 (1999) 203–264.

[53] M. Sirajuddin, S. Ali, V. McKee, S. Zaib, J. Iqbal, Organotin (IV) carboxylate derivatives as a new addition to anticancer and antileishmanial agents: design, physicochemical characterization and interaction with Salmon sperm, RSC Adv., 4 (2014) 57505–57521.

[54] A. W. Addison, T. N. Rao, J. Reedijk, J. van Rijn and G. C. Verschoor, Synthesis, structure, and spectroscopic properties of copper (II) compounds containing nitrogen–sulphur donor ligands; the crystal and molecular structure of aqua [1, 7-bis (N-methylbenzimidazol-2′-yl)-2, 6-dithiaheptane] copper (II) perchlorate, J. Chem. Soc. Dalton Trans., (1984) 1349-1356.

[55] E. R. T. Tiekink, Structural chemistry of organotin carboxylates: a review of the crystallographic literature, Appl. Organom. Chem., 5 (1991) 1-23.

[56] R. Willem, I. Verbruggen, M. Gielen, M. Biesemans, B. Mahieu, T.S. Basu Baul and E.R.T. Tiekink, Correlating Mössbauer and solution-and solid-state 117Sn NMR data with X-ray diffraction structural data of triorganotin 2-[(E)-2-(2-hydroxy-5-methylphenyl)-1-diazenyl] benzoates, Organometallics, 17 (1998) 5758-5766.

[57] C. A. Lipinski, F. Lombardo, B. W. Dominy and P. J. Feeney, Experimental and computational approaches to estimate solubility and permeability in drug discovery and development settings, Adv. Drug. Deliv. Rev., 23 (1997) 3–25.

[58] A. K. Ghose, V. N. Viswanadhan and J. J. Wendoloski, A knowledge-based approach in designing combinatorial or medicinal chemistry libraries for drug discovery. 1. A qualitative and quantitative characterization of known drug databases, J. Comb. Chem., 1 (1999) 55–68.

[59] D. F. Veber, S. R. Johnson, H. Y. Cheng, B. R. Smith, K. W. Ward and K. D. Kopple, Molecular properties that influence the oral bioavailability of drug candidates, J. Med. Chem., 45 (2002) 2615–2623.

[60] W. J. Egan, K. M. Merz and J. J. Baldwin, Prediction of drug absorption using multivariate statistics, J. Med. Chem., 43 (2000) 3867–3877.

[61] I. Muegge, S.L. Heald and D. Brittelli, Simple selection criteria for drug-like chemical matter, J. Med. Chem., 44 (2001) 1841–1846.

[62] F. Lovering, J. Bikker and C. Humblet, Escape from flatland: increasing saturation as an approach to improving clinical success, J. Med. Chem., 52 (2009) 6752–6756.

[63] J. S. Delaney, ESOL: estimating aqueous solubility directly from molecular structure, J. Chem. Inf. Model., 44 (2004) 1000–1005.

[64] Y. C. Martin, A bioavailability score, J. Med. Chem., 48 (2005) 3164–3170.

[65] R. O. Potts and R. H. Guy, Predicting skin permeability, Pharm. Res., 9 (1992) 663–669.